CRIPTO-based micro-heterogeneity of mouse muscle satellite cells enables adaptive response to regenerative micro-environment

Ombretta Guardiola[1,2,*], Francescopaolo Iavarone[1,2], Chiara Nicoletti[3], Maurizio Ventre[4,5], Cristina Rodríguez[1,2], Laura Pisapia[2], Gennaro Andolfi[1,2], Valentina Saccone[6,7], Eduardo J. Patriarca[1,2], Pier Lorenzo Puri[3], Gabriella Minchiotti[1,2,8,*]

[1]Stem Cell Fate Laboratory, Institute of Genetics and Biophysics "A. Buzzati-Traverso", CNR, Naples, 80131, Italy.

[2]Institute of Genetics and Biophysics "A. Buzzati-Traverso", CNR, Naples, 80131, Italy.

[3]Development, Aging and Regeneration Program, Sanford Burnham Prebys Medical Discovery Institute, La Jolla, CA, 92037, USA.

[4]Department of Chemical, Materials and Industrial Production Engineering, University of Naples Federico II, Naples, 80125, Italy.

[5]Center for Advanced Biomaterials for Healthcare@CRIB, Istituto Italiano di Tecnologia, Naples, 80125, Italy,

[6]IRCCS Fondazione Santa Lucia, Rome, 00143, Italy.

[7]Department of Life Sciences and Public Health, Università Cattolica del Sacro Cuore, Rome, 00168, Italy

[8]Lead Contact

Summary

Skeletal muscle repair relies on heterogeneous population of satellite cells (SCs). The mechanisms that regulate SC homeostasis and state transition during activation are currently unknown. Here we investigated the emerging role of non-genetic micro-heterogeneity, *i.e.,* intrinsic cell-to-cell variability of a population, in this process. We demonstrate that micro-heterogeneity of the membrane protein CRIPTO in mouse activated SCs (ASCs) identifies metastable cell states that allow a rapid response of the population to environmental changes. Mechanistically, CRIPTO

*Correspondance to: ombretta.guardiola@igb.cnr.it (O.G.); gabriella.minchiotti@igb.cnr.it (G.M.).

Declaration of Interests
The authors declare no competing interests.

micro-heterogeneity is generated and maintained through a process of intracellular trafficking coupled with active shedding of CRIPTO from the plasma membrane. Irreversible perturbation of CRIPTO micro-heterogeneity affects the balance of proliferation, self-renewal and myogenic commitment in ASCs, resulting in increased self-renewal *in vivo*. Our findings demonstrate that CRIPTO micro-heterogeneity regulates the adaptative response of ASCs to microenvironmental changes, providing insights into the role of intrinsic heterogeneity in preserving stem cell population diversity during tissue repair.

eTOC blurb

Guardiola et al. investigate intrinsic cell-to-cell variability in mouse activated satellite cell (ASC) population in skeletal muscle regeneration. ASCs display a continuum of metastable cell states along with CRIPTO expression gradients, whose dynamic fluctuation enables rapid adaptation to changing microenvironment and preserves muscle stem cell population diversity.

Graphical Abstract
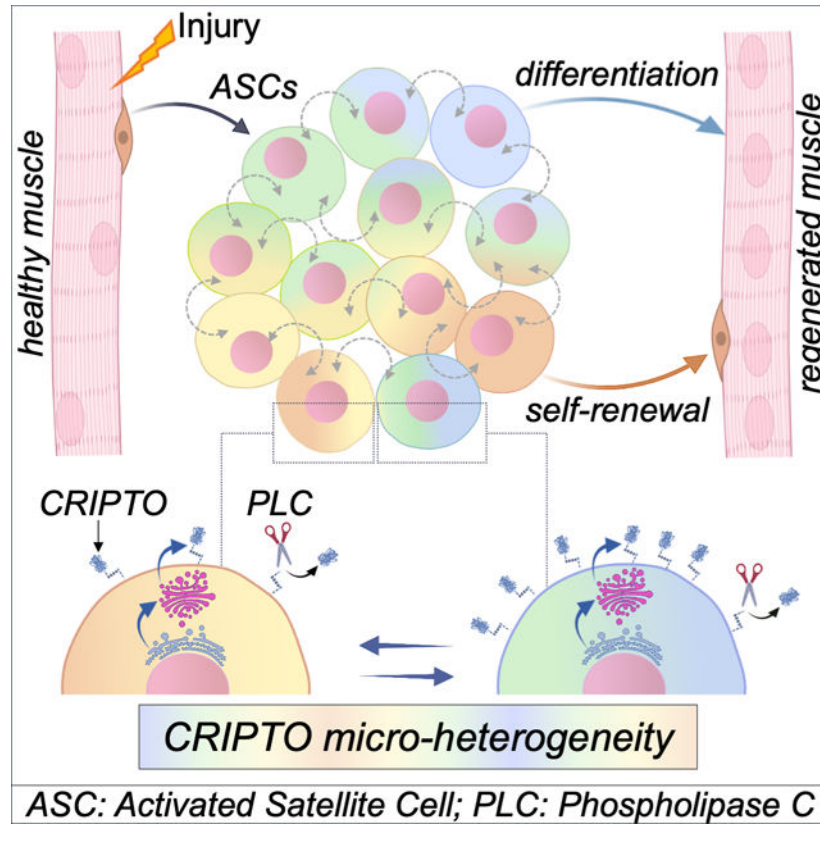
Introduction

Adult satellite cells (SCs) constitute a functional heterogeneous population of muscle stem cells essential for skeletal muscle homeostasis and regeneration throughout life. SC functional heterogeneity results in cell subpopulations with different stemness and myogenic potentials, proliferation rates, modes of division and transcriptomic profiles[1–5]. Under

regenerative pressure, this heterogeneity ensures both long-term maintenance of the SC population and recovery of muscle architecture[6–8], through a finely tuned balance between self-renewal, proliferation rate and differentiation.

Increasing evidence suggests that intermediate reversible cell states exist in stem cell populations, including muscle stem cells in quiescence or aging, to facilitate cell state transition[9–14]. These findings are consistent with the emerging role of intrinsic non-genetic heterogeneity in both physiological and pathological conditions[15–19]. This refers to cell-to cell variability within an isogenic cell population and may arise either from stochastic events, environmental cues or random fluctuation in gene expression[18,19]. Non-genetic heterogeneity can be described as either macro- or micro- heterogeneity[20,21]. Macro-heterogeneity, is characterized by a multimodal distribution of a measurable property (e.g., the expression level of a given gene/protein) that marks distinct subpopulations. Conversely, micro-heterogeneity is intrinsically dynamic, as it refers to small variations of a given trait and it appears as a continuous, single bell-shaped curve [20,22]. Micro-heterogeneity may result in phenotypic, molecular or functional variants that give rise to alternative events or to stochastic processes, both driving cell fate decisions, as for instance the cell fate determination of dystrophic fibro/adipogenic progenitors or the dysfunctionality of aged muscle stem cells[17,23].

However, whether and how non-genetic micro-heterogeneity is involved in regulating the balance between self-renewal and myogenic potentials of Activated SCs (ASCs) during skeletal muscle regeneration, and the underlying cellular mechanisms remains currently unclear.

The present study focuses on the glycosylphosphatidylinositol (GPI)-anchored CRIPTO protein, a TGF superfamily coreceptor. CRIPTO is expressed in activated and proliferating SCs after acute skeletal muscle injury, while it is undetectable in quiescent SCs[24]. Genetic ablation of *Cripto* in the SCs compartment compromises myofiber regeneration, whereas its over-expression promotes myogenic commitment and differentiation and enhances muscle regeneration[24,25]. CRIPTO is emerging as a key regulator of functional heterogeneity of pluripotent and cancer stem cells. Indeed, it has been recently shown that dynamic fluctuations of CRIPTO levels correlates with different functional states in these cell populations, thereby controlling self-renewal and clonogenicity of pluripotent and cancer stem cells, respectively[26–28]. Specifically, fluctuations in levels of CRIPTO expression have been described in mouse embryonic stem cells (ESCs) and in patient-derived colorectal cancer (CRC) stem/progenitor cells[26,27]. These fluctuations parallel those observed for stemness factors and associated with changes of the clonogenic capacity of CRC stem/progenitor cells at the population level[27]. Furthermore, oscillations of CRIPTO mainly correspond with variations in the subcellular/extracellular distribution of the protein rather than changes in RNA expression levels[27]. A similar heterogeneous and fluctuating expression of membrane CRIPTO has been described in mouse ESCs, which positively correlates with the metastable expression of key pluripotency transcription factors and occurs despite negligible variations of the transcript[26]. However, whether CRIPTO exerts similar control over the muscle stem cells heterogeneity, has not yet been investigated.

Here we identify a previously unappreciated micro-heterogeneity of surface CRIPTO in activated SCs (ASCs). We demonstrate that its dynamic fluctuation identifies a continuum of functional metastable states that enable a rapid response of the ASC population to environmental changes before their progression towards irreversible fates. Furthermore, we demonstrate that irreversible perturbation of CRIPTO expression gradient destabilizes the balance between self-renewal and myogenic commitment, suggesting that preserving CRIPTO expression gradient is required to maintain the functional heterogeneity of the ASC population.

Results

CRIPTO micro-heterogeneity identifies distinct phenotypic and molecular cell variants of Activated Satellite Cells (ASCs)

We first investigated the expression pattern of CRIPTO on the surface of Activated Satellite Cells (ASCs), isolated from hind-limb muscles of Tg:Pax7-nGFP reporter mice[29] at day 3 post-Cardiotoxin (CTX) injury (3 dpi), when ASCs exhibit high degree of phenotypic heterogeneity and plasticity[30,31]. Injured muscles were enzymatically digested, and unfixed bulk muscle cells were stained with anti-CRIPTO antibodies (aCRIPTO-APC) (Figure 1A). Flow cytometry analysis was performed by gating the GFP+ ASC pool, and identified a continuous distribution of aCRIPTO-APC fluorescence intensity (Figure 1B) and a single bell-shaped curve with a large breadth (Figure 1C). This expression profile predicts micro-heterogeneity of surface CRIPTO levels within the ASC population[20,32]. Cell-to-cell variability of surface CRIPTO expression was also confirmed by double immunofluorescence staining on freshly isolated GFP+ ASCs, with CRIPTO and the membrane marker Sambucus Nigra Lectin (SNA) (Figure 1D and S1A).

The micro-heterogeneity of surface CRIPTO levels may alternatively reflect different cellular states, presence of discrete cell subpopulations with distinct functional properties, or even random fluctuations in protein expression[19,32]. To address this issue, we first analysed the Side Scatter (SSC) flow cytometry parameter which measures internal cell complexity and serves as a proxy of cell activation states[33,34]. First, we measured the SSC values of the GFP+ ASC population before CTX injury (day 0) and at different time points post injury (from 18 to 72 hours), and found a progressive increase over time (Figure S1B, C). We then analysed the SSC mean values of cells that either express (CRIPTO^{Pos}) or not express (CRIPTO^{Neg}) CRIPTO on the surface of the cell membrane, and those of cell fractions with intermediate surface CRIPTO expression levels (CRIPTO^{IntI} and CRIPTO^{IntII}), each corresponding to ~25% of the total GFP+ population (Figure 1E and Figure S1D). SSC values varied along with CRIPTO expression levels, with the CRIPTO^{Neg} cell fraction showing the lowest SSC value (3.2-times lower than CRIPTO^{Pos}; p<0.0005; Figure 1F, G), suggesting that different levels of surface CRIPTO correlate with distinct cell activation states within the ASC pool.

To gain further insight into these findings, we analysed phenotypic and molecular features of freshly isolated CRIPTO^{Neg} and CRIPTO^{Pos} ASC fractions (Figure 1H). We first assessed mitochondrial activity of the two cell fractions by Mito Tracker staining. FACS analysis showed lower fluorescence intensity in CRIPTO^{Neg} compared to CRIPTO^{Pos} cells,

suggesting a lower energetic demand of this cell fraction (Figure 1I). Furthermore, the global level of 5-hydroxymethylcytosine (5hmC), which positively correlates with active transcriptional activity[35], was significantly lower in CRIPTO[Neg] compared to CRIPTO[Pos] cells, suggesting lower levels of gene expression (Figure 1J). Furthermore, flow cytometry cell cycle analysis by propidium iodide DNA staining showed an accumulation of CRIPTO[Neg] cells in G0/G1 phase and a delayed G1-to-S phase transition, as compared to CRIPTO[Pos] cells (Figure 1K).

Furthermore, we explored whether the phenotypic variances between CRIPTO[Neg] and CRIPTO[Pos] ASCs correlated with distinct transcriptional landscapes. Principal Component Analysis (PCA) from RNA-seq data showed that CRIPTO[Neg] and CRIPTO[Pos] SC fractions clustered separately on the major principal component (Figure 2A). Interestingly, the majority of the differentially expressed genes (DEGs) between CRIPTO[Neg] and CRIPTO[Pos] cells (1193, FDR< 0.05; Supplemental Table 1) consisted of downregulated genes in CRIPTO[Neg] cells, with only 57 genes upregulated in this cell fraction (Figure 2B). We performed Gene Ontology analysis using DAVID and categorized the DEGs in two functional groups: Cellular Component (CC) and Biological Process (BP). Analysis of CC showed that the most statistically significant terms are associated with the extracellular region, membrane, extracellular space and other functions related to the external side of the plasma membrane (Figure 2C). This suggested that different levels of surface CRIPTO correlate with rearrangements of extracellular molecules. The top ten terms in BP category showed that most of DEGs were mainly enriched in immune system process and inflammatory response, as well as chemotaxis, cell adhesion and extravasation (Figure 2D). Accordingly, a parallel Gene Set Enrichment Analysis (GSEA) analysis showed a significant enrichment of genes related to inflammatory response, migration and cell surface interactions in CRIPTO[Pos] cells (Figure 2E, F and S2A). These differences in gene expression suggest that the increased CRIPTO levels typically observed in ASCs might confer responsiveness to signals derived from environmental sources, such as immune cells and extracellular matrix. In contrast, CRIPTO[Neg] cells were enriched in gene sets related to energy metabolism (alteration in TCA, complex I, OXPHOS, mitochondrial translation), cholesterol contents/membrane fluidity and mRNA transcription and splicing (Figure 2E and G and S2B).

Previous works showed that different expression levels of PAX7 define SC heterogeneity with high levels of PAX7 (PAX7[High]) in SCs that display a lower metabolic activity and are less primed for commitment, as compared to the PAX7[Low] counterpart[1,36]. We therefore investigated whether the CRIPTO distribution correlated with the hierarchical organization of SC subpopulations, as defined by PAX7 expression levels. To this purpose, we assessed the association between CRIPTO and GFP (PAX7) expression in PAX7[High] and PAX7[Low] subpopulations isolated from Tg:Pax7-nGFP mice (Figure 2H, I), as well as in CRIPTO[Pos] cells (Figure S2C). Linear correlation analysis of the Mean Fluorescence Intensity (MFI) showed no significant relationship between CRIPTO and GFP expression levels. These results were further corroborated by staining of freshly isolated CRIPTO[Pos] and CRIPTO[Neg] cells with PAX7 antibodies (Figure S2D), which showed heterogeneous expression of PAX7 in both cell fractions.

Taken together, these results indicate that micro-heterogeneity of surface CRIPTO identifies phenotypic and molecular variants within the ASCs population, which do not correlate with SCs subpopulations, as defined by PAX7 expression levels.

CRIPTO^{Pos} and CRIPTO^{Neg} -ASC fractions exhibit different functional properties *in vitro*

We next investigated biological properties of CRIPTO^{Pos} and CRIPTO^{Neg} ASCs, by assessing their self-renewal, proliferative and myogenic potential *in vitro*. To this end, the two freshly isolated cell fractions were plated at low density on Matrigel-coated plates in growth medium (Figure 3A). Following an overnight culture, the resulting cells were stained with specific antibody combinations that identify discrete populations of myogenic cells, including PAX7/KI67, GFP/MYOD, and MYOD/MYOG double positive cells. Quantification of PAX7±/KI67± cell distribution showed a significant increase of non-proliferating PAX7+/KI67− cells in CRIPTO^{Neg}, as compared to CRIPTO^{Pos}-derived cells (41.4±3.1% in CRIPTO^{Neg} cells *vs* 20.3±4.7% in CRIPTO^{Pos} cells; $p<0.05$; Figure 3B, C). Quantification of GFP±/MYOD± cell distribution, showed that the fraction of self-renewing (GFP+/MYOD±) cells was significantly higher in CRIPTO^{Neg} compared to CRIPTO^{Pos}-derived cells (33.2±2.6% in CRIPTO^{Neg} cells *vs* 19.06±3.5% in CRIPTO^{Pos} cells; $p<0.05$; Figure 3D). Conversely, myogenic committed GFP+/MYOD+ cells were significantly enriched in the CRIPTO^{Pos}-derived population compared to CRIPTO^{Neg}-derived cells (78.6±3.6% in CRIPTO^{Pos} *vs* 63±4.3% in CRIPTO^{Neg} cells; $p<0.05$; Figure 3D). We found no differences in the proportion of differentiating MYOD+/MYOG+ cells between the two cell fractions (5.8±1.9% in CRIPTO^{Pos} *vs* 3.83±0.6% in CRIPTO^{Neg} cells; p=ns; Figure 3E).

We then analysed both the duration of cell division and the migratory properties of the two cell fractions by time-lapse video microscopy (Figure 3A). The duration of the mitotic division events was measured as the interval between the mitotic entry, namely the adoption of a spherical shape[37,38], and the appearance of the first morphological evidence of cytokinesis, which is characterized by the appearance of a cleavage furrow on the cell surface (Figure 3F; Videos S1 and S2). CRIPTO^{Neg} cells showed a significant slowdown in the duration of mitotic division, when compared to CRIPTO^{Pos} cells (Figure 3G), with a lower fraction of daughter cells entering a second round of division during the 20-hours time-lapse (4.2±0.8% of CRIPTO^{Neg} *vs* 10.2±1.5% of CRIPTO^{Pos} daughter cells; $p<0.005$; Figure 3H). Cell tracking analysis showed no significant differences in cell directionality between the two populations, as indicated by the individual cell trajectory plots (Figure 3I). However, CRIPTO^{Neg} cells exhibited a significant increase in persistence time and a lower velocity (RMS speed), as compared to CRIPTO^{Pos} cells (Figure 3J, K).

Overall, these data indicate that CRIPTO^{Neg} and CRIPTO^{Pos} cells exhibit distinct functional properties upon *in vitro* culture. Specifically, while CRIPTO^{Neg}-derived cells showed a slower cell cycle progression rate and a higher propensity to self-renew, CRIPTO^{Pos}-derived cells were more prone to proliferation, migration and myogenic commitment.

CRIPTO[Pos] and CRIPTO[Neg] ASCs exhibit similar regenerative potential *in vivo*

We then assessed the behaviour of CRIPTO[Pos] and CRIPTO[Neg] cell fractions in a regenerative environment *in vivo*. To allow lineage tracing of both cell fractions, and analyse their contribution to muscle regeneration and replenishment of the satellite cell pool, we generated the Tg:Pax7-nGFP::$R26^{mTmG}$ reporter mice by crossing the Pax7-nGFP mice and the $R26^{mTmG}$ (membrane Tomato-stop-membrane GFP) reporter line[39], which constitutively expresses a membrane tdTomato fluorescent protein (tdTomato). CRIPTO[Pos] and CRIPTO[Neg] ASCs were FACS-isolated from hind limb muscles of the Tg:Pax7-nGFP:: $R26^{mTmG}$ mice at 3 dpi and subsequently transplanted in CTX-injured Tibialis Anterior (TA) muscles of wild type C57BL/6J recipient mice (Figure 4A). Four weeks after transplantation, muscle sections were double stained with antibodies against LAMININ and GFP, and the number of tdTomato positive myofibers and GFP positive SCs derived from CRIPTO[Pos] and CRIPTO[Neg] transplanted cells were quantified (Figure 4B). The number of tdTomato expressing myofibers and GFP+ cells were both comparable in the two groups of mice (Figure 4B-D). These findings suggested that both CRIPTO[Pos] and CRIPTO[Neg] transplanted cells exhibit comparable regenerative potential *in vivo*.

Therefore, we asked whether these cell fractions represent dynamic or stable subpopulations. Dynamic and reversible cell states can be identified when isolated cell fractions within a heterogeneous population are capable of repopulating each other over time or in different conditions, while the inability to reconstitute the naive distribution suggests the presence of stable subpopulations, as previously described[20,32]. We thus assessed whether ASCs derived from CRIPTO[Pos] and CRIPTO[Neg] transplanted cells were able to restore CRIPTO micro-heterogeneity by repopulating each other or maintain CRIPTO expression levels of the freshly isolated cells[20,32]. To address this issue, freshly isolated CRIPTO[Pos] and CRIPTO[Neg] ASCs from Tg:Pax7-nGFP mice were transplanted in CTX-injured muscles of C57BL/6J wildtype recipient mice. Four weeks after transplantation, the muscles were re-injured to activate the SC population and CRIPTO expression was assessed in ASCs at 3dpi (Figure 4E). FACS analysis of GFP+ASCs derived from both CRIPTO[Pos] and CRIPTO[Neg] transplanted cells showed a heterogeneous distribution of CRIPTO, compared to that of the donor cells (Figure 4F, G), thus indicating that both CRIPTO[Pos] and CRIPTO[Neg] cell fractions were able to repopulate each other *in vivo*.

Our findings indicate that CRIPTO[Pos] and CRIPTO[Neg] ASCs exhibit similar regenerative potential and can reconstitute the naïve distribution of CRIPTO *in vivo*, suggesting a dynamic and reversible nature of the two cell populations.

Phospholipase C-mediated active protein shedding regulates CRIPTO micro-heterogeneity in ASCs

The ability of CRIPTO[Pos] and CRIPTO[Neg] ASCs to restore CRIPTO micro-heterogeneity prompted us to investigate the underlying cellular mechanism. To address this issue, we first investigated the ability of CRIPTO[Pos] and CRIPTO[Neg] cells to repopulate each other *in vitro*. Both cell fractions were isolated from Tg:Pax7-nGFP mice at 3 dpi, incubated for 2 hours at room temperature (RT) in low serum, and re-stained with aCRIPTO-APC antibody (Figure S3A, line a). FACS analysis showed that both aCRIPTO[Pos] and CRIPTO[Neg] cell

fractions could efficiently repopulate each other *in vitro*, indicating they both reconstitute the naïve CRIPTO microheterogeneity (Figure S3B, C). *Cripto* RNA levels were comparable in CRIPTO[Pos] and CRIPTO[Neg] cell fractions (Figure S3D), suggesting that post-transcriptional or post-translational regulation may control the dynamic regulation of CRIPTO. CRIPTO is anchored to the cell membrane via a glycosylphosphatidylinositol (GPI) anchor, and can be either internalized[40,41] and/or actively shed from the membrane by phospholipase (PL) A_2, C and/or D enzymes[42–44]. We thus hypothesized that the reconstitution of CRIPTO micro-heterogeneity might results from internalization and/or shedding of the protein. To determine whether CRIPTO is internalized or shed from the membrane, we took advantage of the property of the protein/antibody complex (e.g., the complex used for sorting the CRIPTO[Pos] cells) that continues to emit fluorescence, once internalized. Conversely, shedding of the protein/antibody complex leads to the loss of fluorescent signal[45]. To further address this issue, freshly isolated GFP+ CRIPTO[Pos] and CRIPTO[Neg] cells were cultured at RT in low serum and either stained or not with aCRIPTO-APC antibody, before FACS analysis (Figure 5A, line a). The APC fluorescent signal was almost completely absent in the unstained cells (Figure 5B and D). CRIPTO[Pos] cells that were stained with aCRIPTO-APC antibody showed the expected heterogeneous distribution of the fluorescent signal (Figure 5B). These results suggested that the restoration of CRIPTO heterogeneity is likely due to protein shedding rather than internalization. To further explore this hypothesis, we used specific inhibitors of the different PL enzymes, including Varespladib (LY-315920) for PLA_2, U73122 for PLA2, and PLC, and 5-Fluoro-2-indolyl deschlorohalopemide (FIPI) for PLD. CRIPTO[Pos] cells were thus incubated at RT with either PL inhibitors or DMSO as Control, stained with aCRIPTO-APC antibody and analysed by FACS (Figure 5A, line b). U73122-treated CRIPTO[Pos] cells-derived population failed to properly reconstitute the naïve CRIPTO intensity distribution compared to control (Figure 5C), and accumulated CRIPTO at the cell membrane. Conversely, neither Varespladib or FIPI prevented the restoration of CRIPTO heterogeneity, suggesting that CRIPTO shedding was mainly regulated by the activity of PLC, at least in our experimental conditions (Figure S3A, line b and S3E).

Finally, we tested the effects of the PL enzymes inhibitors on CRIPTO[Neg] cell fraction using the same experimental setting (Fig. 5A). As expected, CRIPTO[Neg] cells were able to reconstitute CRIPTO heterogeneity (Figure 5D). Treatment of CRIPTO[Neg] cells with U73122 resulted in CRIPTO accumulation at the cell membrane, preventing the restoration of naïve distribution of the protein (Figure 5E). Conversely, both Varespladib and FIPI-treated CRIPTO[Neg] cells reconstituted CRIPTO heterogeneity similar to control (Figure S3A, line b and S3F).

Together these results indicate that CRIPTO micro-heterogeneity in ASCs is regulated through active shedding of the protein from the plasma membrane, and suggest that this process is mainly mediated by the phospholipase C activity.

One-way membrane trafficking of CRIPTO reconstitutes CRIPTO micro-heterogeneity in ASC population

CRIPTO undergoes extensive post-translational modifications and trafficking through the Endoplasmic Reticulum (ER) and Golgi apparatus before being exported to the

cell surface[41,42]. These observations, along with our findings that U73122 treatment rapidly converts CRIPTO[Neg] cells to CRIPTO[Pos] (Figure 5E), raised the hypothesis that reconstitution of CRIPTO heterogeneity may involve intracellular trafficking of CRIPTO and rapid translocation of the protein to the cell membrane. To investigate this possibility, we first assessed the presence of intracellular storage of CRIPTO in the ASCs. To this end, freshly isolated CRIPTO[Neg] and CRIPTO[Pos] cell fractions (Figure 5F and S4C) were either permeabilized or left untreated before CRIPTO and Phalloidin staining, used as intracellular marker. FACS analysis showed a heterogeneous distribution of CRIPTO in Phalloidin-positive cells, which was comparable in the two cell fractions regardless of surface CRIPTO levels (Figure 5G and S3G). To investigate the intracellular localization of the protein, we performed double immunostaining with CRIPTO and the ER marker Prolyl 4-Hydroxylase Subunit Beta (P4HB) on both permeabilised CRIPTO[Neg] and CRIPTO[Pos] cells. Immunofluorescence analysis showed the co-localization of the two proteins within the ER (Figure 5H and S3H, respectively). We thus investigated whether inhibition of intracellular membrane trafficking in CRIPTO[Neg] cells may affect the reconstitution of CRIPTO micro-heterogeneity. To this end, freshly isolated CRIPTO[Neg] cells were incubated at 20°C to block protein transport from the trans-Golgi network to the cell surface[46], either alone or in the presence of the microtubule inhibitor Nocodazole (Noc)[47] and stained with aCRIPTO-APC antibodies for FACS analysis (Figure 5I, line a). The restoration of naïve CRIPTO distribution was reduced at 20°C (Figure 5K), as compared to RT (Fig. 5J), and was further affected by Noc treatment (Figure 5L), suggesting that the reconstitution of CRIPTO micro-heterogeneity depends on protein trafficking and translocation to the extracellular space. Finally, we treated CRIPTO[Neg] cells with U73122 at 20°C to interfere with both CRIPTO export to- and shedding from- the plasma membrane (Figure 5I, line b), which resulted in a significant increase of CRIPTO[Pos] cells (64.7±6% 20°C+U73122 vs 30.4±2.4% 20°C+DMSO) (Figure 5M and Figure S3I, J). These results suggested that a subset of cells that escape the inhibition of protein trafficking translocate CRIPTO at the plasma membrane where it accumulated due to the inhibitory effect of U73122.

Collectively, these data indicate that the regulation of CRIPTO microheterogeneity in ASC population is regulated through a one-way mechanism of intracellular protein trafficking and translocation of CRIPTO to the extracellular space coupled to active protein shedding from the plasma membrane.

Irreversible perturbation of CRIPTO micro-heterogeneity affects ASC behaviour

To investigate the functional role of CRIPTO micro-heterogeneity in the ASCs population, we assessed the consequence of disrupting this dynamic heterogeneity using a genetic knock-out approach to induce a permanent CRIPTO[Neg] state in the ASCs. To this end, we generated the *Tg:Pax7-CreERT2::R26[mTmG]::Cripto[loxP/-]* (*Cripto[-cKO]*) mice, by crossing the *R26[mTmG]* reporter mice with the *Tg:Pax7-CreERT2::Cripto[loxP/-]* mice[24] (Figure S4A). In these transgenic mice, tamoxifen (tmx)-inducible Cre-mediated recombination in PAX7 expressing SCs leads to the simultaneous deletion of *Cripto* and *tdTomato* along with expression of GFP (Figure 6A), allowing lineage tracing of control (*Cripto[-wt]*) and *Cripto[-cKO]* cells. The Cre-mediated recombination of the different alleles was confirmed

by PCR genotyping of skeletal muscles (Figure S4B) and FACS analysis of recombinant *Cripto*$^{-cKO}$ and *Cripto*$^{-wt}$ GFP positive cells (Figure S4C).

To investigate the behaviour of *Cripto*$^{-cKO}$ cells, we first assessed the contribution of transplanted *Cripto*$^{-cKO}$ and *Cripto*$^{-wt}$ ASCs to myofiber regeneration and to the replenishment of the satellite cell pool *in vivo*. To this end, GFP+ASCs were FACS isolated from hind limb muscles of tmx-treated *Cripto*$^{-wt}$ and *Cripto*$^{-cKO}$ mice at 3 dpi and immediately transplanted into injured TA muscles of C57BL/6J wild type recipient mice (Figure 6A). Four weeks after transplantation the GFP positive myofibers were analysed in muscle sections. Both *Cripto*$^{-cKO}$ and *Cripto*$^{-wt}$ cells generated mosaic muscles with comparable number of GFP positive myofibers (Figure 6B, C), indicating that transplanted *Cripto*$^{-cKO}$ cells were able to fuse into new myofibers. However, unlike what we observed with CRIPTO^{Neg} cells (Figure 4B, D), quantification of PAX7+/GFP± cell distribution showed a ~2-fold increase of PAX7+/GFP+ cells in the muscles transplanted with *Cripto*$^{-cKO}$, as compared to *Cripto*$^{-wt}$ cells (13.3±0.1% from donor *Cripto*$^{-cKO}$ vs 6.6±0.5% from donor *Cripto*$^{-wt}$; p<0.0005; Figure 6K), indicating different regenerative potential.

To further characterize these cells, we analysed the cell cycle progression of *Cripto*$^{-cKO}$ vs *Cripto*$^{-wt}$ cells. To this end, GFP+ASCs were isolated from hind limb muscles of tamoxifen (tmx)-treated *Cripto*$^{-cKO}$ and *Cripto*$^{-wt}$ mice at 3 dpi and analysed by FACS after propidium iodide staining (Figures 6E). *Cripto*$^{-cKO}$ cells were predominantly in G0/G1 phase and showed a reduced G1-to-S phase transition compared to *Cripto*$^{-wt}$ cells (Figures 6F). This phenotype was similar to that of CRIPTO^{Neg} cell fraction (Figure 4E), confirming that absence of *Cripto* is associated with a lower proliferation rate, as compared to transiently-amplifying wildtype ASCs. To further investigate this phenotype, we isolated single fibers from resting Extensor Digitorum Longus (EDL) muscles of tamoxifen-treated *Cripto*$^{-cKO}$ and *Cripto*$^{-wt}$ mice and analysed the fiber-associated ASCs (Figure 6G). After 44 hours in culture in growth medium, fibers were labelled by a short pulse of EdU (4 hours), and stained for GFP and EdU (Figure 6G, line a). Quantification analysis showed that the percentage of GFP+/EdU+ ASCs was significantly lower in single fibers isolated from *Cripto*$^{-cKO}$, as compared to *Cripto*$^{-wt}$ mice (38.6±3.6% from *Cripto*$^{-cKO}$ vs 68.0±6.2% from *Cripto*$^{-wt}$; p<0. 05; Figure 6H, I), confirming a reduced propensity of *Cripto*$^{-cKO}$ cells to enter the S phase of the cell cycle. Furthermore, we used the asymmetric activation of p38α/β MAPK as a readout of myogenic commitment[48]. To this end, single myofibers were cultured for 24 hours in GM and stained for p38α/β MAPK (Figure 6G, line b). We evaluated the symmetric vs asymmetric localization of phospho-p38α/β (pp38) in dividing GFP+ ASC pairs, as identified by two connected cells with a cleavage furrow on the cell surface (Figure 6J). The percentage of ASC pairs with asymmetric distribution of pp38 was almost doubled in *Cripto*$^{-cKO}$ compared to *Cripto*$^{-wt}$-derived single fibers (23.6±1.7% from *Cripto*$^{-cKO}$ vs identify.7±2.0% from *Cripto*$^{-wt}$; p<0. 05; Figure 6K), suggesting that *Cripto*$^{-cKO}$ daughter SCs have a higher propensity for self-renewal.

These data indicate that ASCs that are forced into a permanent CRIPTO^{Neg} state do not retain the ability to self-organize into the typical micro-heterogeneity of ASCs and suggest this affects cell fate determination by increasing ASC propensity to self-renewal.

CRIPTO micro-heterogeneity preserves the balance between self-renewal and myogenic commitment

To further investigate if CRIPTO micro-heterogeneity is required to regulate the ASCs *in vivo*, we analysed muscle sections from *Cripto^{-cKO}* and *Cripto^{-wt}* mice during muscle regeneration (Figure S4D). The morphometric analysis showed a significant reduction of the mean Cross-Sectional Area (CSA) values of *Cripto^{-cKO}* compared to *Cripto^{-wt}* mice at 15 dpi, which persisted at 30 dpi, and was recovered/compensated at 60 dpi (Figure S4E, F). The average distribution of GFP positive myofibers was comparable between the two groups at 30 dpi (76.7±23.7% in *Cripto^{-cKO}* *vs* 96.0±1.2% in *Cripto^{-wt}*; *p*=NS; Figure S4G, H), indicating that *Cripto^{-cKO}* cells were able to fuse into new myofibers. However, the CSA distribution of GFP+ myofibers showed a significant shift towards smaller sizes in *Cripto^{-cKO}*, as compared to *Cripto^{-wt}* muscles (Figure S4I), thus confirming and extending our previous findings[24].

We thus assessed the self-renewal capacity of *Cripto^{-cKO}* vs *Cripto^{-wt}* cells, and first analysed the distribution of PAX7+/GFP± cells at 30 dpi. Recombinant PAX7+/GFP+ SCs nearly doubled in *Cripto^{-cKO}* muscles compared to *Cripto^{-wt}* (72.8±6.0% in *Cripto^{-cKO}* *vs* 45.3±5.0% in *Cripto^{-wt}* muscles; *p*<0.05). No significant difference was observed in the frequency of non-recombinant PAX7+/GFP-SCs (Figure 7A, upper and lower panels). Furthermore, double staining with PAX7 and KI67 showed that the number of non-cycling PAX7+/KI67− cells was consistently higher in *Cripto^{-cKO}* mice throughout the whole time-course. Moreover, we found a transient increase of PAX7+/KI67+ cycling cells in *Cripto^{-cKO}* mice at 15 dpi (Figure 7B, C).

To investigate whether the overall increase in PAX7+ cells in *Cripto^{-cKO}* mice was a consequence of a slower/extended proliferative phase and/or of an enhanced self-renewal, we performed dual-labelling experiments. To this end, tmx-treated *Cripto^{-cKO}* and *Cripto^{-wt}* mice were labelled by either a long or short pulse of BrdU after CTX injection and analysed at 15 and 60 dpi, respectively (Figure 7D, G). EdU was administered intraperitoneally (IP) at 24 and 2 hours before sacrifice, in both experimental conditions. For the long-term BrdU labelling (Figure 7D), *Cripto^{-cKO}* and *Cripto^{-wt}* mice were injected IP with BrdU for 10 consecutive days and the muscles were analysed at 15 dpi (Figure 7D). Due to the slow rate of label dilution, both slow dividing and self-renewing cells retained BrdU. Quantification of PAX7+/Brdu± cells showed a significant increase in the frequency of PAX7+/BrdU+ Label-Retaining Satellite Cells (LRSCs)[49] in *Cripto^{-cKO}* vs *Cripto^{-wt}* muscles (27.8±7.0 in *Cripto^{-cKO}* vs 14±3.1.0 in *Cripto^{-wt}* *cells*; p<0.05), while no significant difference was observed in the frequency of NOT-LRSCs PAX7+/BrdU− (Figure 7E). Double staining with PAX7 and EdU showed a strong increase of PAX7+/EdU+ proliferating cells in *Cripto^{-cKO}* compared to *Cripto^{-wt}* muscles (25.5±8 in *Cripto^{-cKO}* *vs* 3.6±1.9 in *Cripto^{-wt}* cells; *p*<0.05; Figure 7F). These data showed that *Cripto^{-cKO}* cells exhibit a slower and prolonged proliferation phase that eventually results in an increased number of PAX7+ cells in Cripto^{-cKO} muscles. To assess whether the overall increase in PAX7+ cells in *Cripto^{-cKO}* muscles was due to sustained proliferation and/or increased self-renewal, we performed a short-term labelling with BrdU. *Cripto^{-cKO}* and *Cripto^{-wt}* mice were injected IP with BrdU for 5 consecutive days after injury, and the muscles were analysed at 60 dpi (Figure 7G).

In this experimental setting, the BrdU-label was mostly retained by self-renewing cells. We found that while the PAX7+/BrdU+ LRSCs were enriched in *Cripto^-cKO* muscles (13.9±3 in *Cripto^-cKO* vs 2.1±0.6 in *Cripto^-wt* cells; $p<0.05$), no significant difference was observed in the frequency of NOT-LRSCs PAX7+/BrdU-cells (Figure 7H, I). Proliferating PAX7+/EdU+ cells were absent in both *Cripto^-cKO* and *Cripto^-wt* mice at this time point (Figure S4J).

Overall, these findings indicate that forcing ASCs in a permanent CRIPTO^Neg state results in increased self-renewal potential and point to a functional role of CRIPTO micro-heterogeneity in preserving the dynamic equilibrium between self-renewal and myogenic commitment in muscle regeneration.

Discussion

Emerging evidence indicate that clonal population of adult stem cells are endowed with non-genetic cell-to-cell variability that can determine differential response and adaptation of the population to varying environmental conditions[19,50]. Whether such non-genetic heterogeneity exists in adult satellite cell (SC) population and their progeny, and how this impacts SC-mediated regeneration of skeletal muscle remains currently unclear.

Here we propose that micro-heterogeneity of surface CRIPTO determines the adaptive response of adult activated SCs (ASCs) to the regenerative microenvironment, and is required to preserve the equilibrium between self-renewal, proliferation and differentiation during early regenerative events. We demonstrate that ASCs in the early phase of skeletal muscle regeneration display a continuum range of CRIPTO levels, which identifies an intrinsic non-genetic heterogeneity of the protein[20]. First, we investigated whether the two cell fractions at the extreme of this continuum (CRIPTO^Pos and CRIPTO^Neg) represent dynamic or stable subpopulations by assessing their ability to repopulate each other; i.e., to reconstitute the heterogeneous distribution of CRIPTO[20,32]. We demonstrate that freshly isolated CRIPTO^Pos and CRIPTO^Neg cell fractions are able to rapidly reconstitute the naïve CRIPTO micro-heterogeneity; thus, suggesting that they are in a dynamic state rather than representing stable subpopulations. In line with their dynamic nature, CRIPTO^Pos and CRIPTO^Neg cells repopulate each other *in vivo* after transplantation in a regenerative microenvironment. Furthermore, transplanted CRIPTO^Pos and CRIPTO^Neg cells equally contribute to muscle regeneration and replenishment of the SC pool, showing similar regenerative potential. Nevertheless, despite their dynamic nature, CRIPTO^Pos and CRIPTO^Neg ASCs show different phenotypic, molecular and functional properties. Several evidences support this hypothesis. First, CRIPTO^Neg cells exhibit a lower mitochondrial and transcriptional activity, when compared to CRIPTO^Pos cells, suggesting a lower energetic demand of this cell fraction. Furthermore, CRIPTO^Neg cells show a slower cell cycle progression rate and a higher propensity to self-renew; whereas, CRIPTO^Pos cells are more prone to proliferation, migration and myogenic commitment. The apparent discrepancy between the behaviour of CRIPTO^Pos and CRIPTO^Neg cells after *in vitro* culture and upon *in vivo* transplantation can be explained by the different microenvironmental conditions *in vitro* and *in vivo*. Specifically, *in vitro* microenvironmental conditions may prevent/delay the rapid adaptive response of the population that conversely occurs *in vivo* under regenerative pressure.

Genome wide analysis of the transcriptional profiles support the idea that CRIPTO[Pos] and CRIPTO[Neg] cells identify different functional states of the ASCs. First, comparative analysis of the differentially expressed genes (DEGs) shows that i) most of DEGs (~95%) are down-regulated in CRIPTO[Neg] cells, and ii) the few DEGs (57) that are upregulated in this cell fraction are enriched in genes expressed and/or upregulated in quiescent cells, including *CalcR, Tenm4, HeyL, Edn3, Wnt4, Fzd4*. In line with the idea that CRIPTO[Neg] cells are in an early activation state, they are enriched in genes associated with oxidative phosphorylation and TCA cycle, and have lower energetic demand. Cellular Component Gene Ontology (GO) analysis shows a significant enrichment in categories associated with extracellular region and space, suggesting that different levels of surface CRIPTO are associated/correlate with dynamic rearrangements of surface proteins. Of relevance, the top most significant Biological Process GO terms and GSEA pathways are associated with cell migration and cell adhesion, and with immune system process and inflammatory response. In particular, CRIPTO[Pos] cell fraction is enriched in genes associated with satellite cell activation and proliferation, including *Mcp-1, Hgf, Igf, Lif, Ngf, Il-1, Il-6* and cell migration and fusion (*Sdf-1, Cxcl14, Il-6*). It is known that many cytokines are secreted by muscle stem cells, but their specific role in skeletal muscle regeneration has not been deeply analysed, yet[51]. Recent findings described the existence of specific cytokine-expressing satellite cell subpopulations, including a so-called 'immunomyoblasts' transitional cell state, which is characterised by immune genes' enriched signature[30,51]. Interestingly, most of the immunomyoblasts enriched genes are upregulated in CRIPTO[Pos] cells, including those involved in immune cell complement activation as *C1qa*, *C1qb*, *C1qc*, major histocompatibility class II antigens as *H2-Eb1*, *H2-Aa*, *H2-Ab1* and members of the cathepsin family (C*tsb*, *Ctss*)[30]. We thus hypothesise that ASCs expressing high level of surface CRIPTO are engaged in the emerging regulatory system that involves muscle-derived cytokines, possibly released by inflammatory cells. This is in line with the idea that cell surface membrane proteins function as interface with the surrounding environment, and can rapidly detect and respond to external cues and information released from the neighbour cells[52]. Based on its activity as modulator of different signalling pathways, including TGFβ and WNT/β catenin, we can speculate that rapid variation of surface CRIPTO levels might modify the sensitivity of the cells to signaling molecules/growth factor/cytokines, which eventually translate in changing of gene expression. Thus, the threshold levels of surface CRIPTO might represent one of the local signalling mediators that allow rapid response of ASCs to changes in the environmental cues.

Of note, CRIPTO microheterogeneity is maintained in ASCs populations expressing either high or low level of PAX7; furthermore, both CRIPTO[Pos] and CRIPTO[Neg] cell fractions show a heterogeneous distribution of Pax7. This leads to hypothesise that the cell variants identified by different surface CRIPTO levels do not correlate with SC subpopulations defined by Pax7 expression levels[1]. Thus, dynamic expression and subcellular distribution of CRIPTO provides an additional layer of regulation independent on the expression level of the genetic marker of SC identity PAX7, thereby supporting the conclusion that CRIPTO micro-heterogeneity provides a non-genetic regulation of SC biology.

Interestingly, cell-to-cell variation of CRIPTO expression does not mainly correlate with variation of the transcripts but rather with variation in subcellular distribution of the protein.

We demonstrate that CRIPTO micro-heterogeneity is regulated by a one-way mechanism of protein trafficking coupled with phospholipase C-dependent active shedding of the protein from the membrane. We propose that this kind of fast cellular mechanism is one of the self-regulating mechanisms that allow adaptation of the ASC population to the regenerative microenvironment, and preserve the functional diversity of the population. In support of our hypothesis, permanent perturbation of CRIPTO micro-heterogeneity in ASCs by *Cripto* genetic ablation affects the dynamic equilibrium between proliferation, self-renewal and myogenic commitment. We show that ASC population that are forced in a permanent/ irreversible CRIPTO[Neg] state (i.e., *Cripto[-cKO]* ASCs) slow down proliferation and increase their propensity to self-renewal. We thus suggest that because of their genetic deficiency, *Cripto[-cKO]* cells do not retain the ability to self-organize into the typical heterogeneity of ASCs. Conversely, CRIPTO[Neg] ASCs, because of their dynamic nature, are able to rapidly restore their naïve state, and this secures the adaptive response of the population to changing in the microenvironment. Indeed, CRIPTO[Neg] ASCs efficiently contribute to regeneration after transplantation, unlike *Cripto[-cKO]* ASCs.

It would be interesting to investigate in future studies if this mechanism is conserved across muscle types of different embryonic origin, including the extra-ocular muscles, which are spared in some muscle disease, such as Duchenne muscular dystrophy, and whether it is susceptible to dysregulation in muscle diseases or aging. It has been shown that muscle stem cells of different embryonic origins have distinct transcriptional myogenic programs, which may explain, at least in part, the specificity of several muscle pathologies that are restricted to specific region of the body [53,54].

The functional role of non-genetic heterogeneity of the stem cell populations is recently emerging in many different contexts[15–17], and it is recently being explored also in the muscle field[23]. Thus, although further evidence is required to consolidate our findings in muscle stem cell population derived from different muscle types, we can speculate that non-genetic heterogeneity, which may also involve other surface proteins, may be a general property of the ASCs population, independently of their origin.

In conclusion, we demonstrate that the propensity to generate and maintain a gradient of surface CRIPTO expression within the ASC pool is an adaptive cellular mechanism occurring at population level that is required to preserve the dynamic heterogeneity of the ASC pool. We propose a model predicting the coexistence of metastable and inter-convertible states in the ASC population that can be regulated by stochastic mechanisms, such as fluctuating levels of surface proteins.

More generally, our findings open further insights into stem cell biology and the significance of intrinsic non-genetic heterogeneity in adult stem cells population response to microenvironmental changes.

Limitations of the study

In this study, we used *Cripto[-cKO]* ASCs to assess the functional consequences of forcing the ASC population towards a permanent CRIPTO[Neg] -like state, although we are aware that *Cripto[-cKO]* do not fully resemble surface CRIPTO[Neg] cell population. This limitation

arises both from the intrinsic dynamic nature of the CRIPTO[Pos] and CRIPTO[Neg] cells, and the lack of inhibitors and/or conditions to selectively perturb CRIPTO trafficking and shedding in ASCs. Furthermore, while our primary focus was investigating the intrinsic cell-to-cell variability alongside CRIPTO expression gradients in ASCs, our transcriptomic dataset showed additional insights on the role of CRIPTO microheterogeneity. Specifically, the intriguing observation that high surface CRIPTO levels correlated with the upregulation of several immune genes, raises questions about the role of non-genetic heterogeneity in mediating the crosstalk between ASCs and inflammatory cells, orchestrating immune responses. This relevant issue remains unaddressed, thus highlighting the need for future research.

STAR Methods

Resource availability

Lead contact—Further information and requests for resources and reagents should be directed to and will be fulfilled by the Lead Contact, G. Minchiotti (gabriella.minchiotti@igb.cnr.it).

Materials availability—Mouse lines generated in this study are available from the Lead Contact by request.

Data and code availability—The RNA-seq transcriptomic that support the findings of this study have been deposited on the Sequence Read Archive (SRA) database and are publicly available. Accession number is listed in the key resources table. Any additional information required to re-analyse the data reported in this paper is available from the Lead Contact upon request.

Experimental model and study participant details

Animals—All experiments in this study were conducted in strict accordance with the institutional guidelines for animal research and approved by the Department of Public Health, Animal Health, Nutrition and Food Safety of the Italian Ministry of Health (authorization number: DM n. 868/2015-PR and 720/2020-PR), in accordance with the law on animal experimentation. All mice were 6–12 weeks old. Tg:Pax7-nGFP[29] were used to analyse CRIPTO[Pos/Neg] cell fractions and transplantation experiments. C57BL/6 and *Tg:Pax7-nGFP::R26^{mTmG}* mice (generated by crossing *Tg:Pax7-nGFP* and the reporter *R26^{mTmG}* (*membrane Tomato-stop-membrane GFP*)[39] were used for transplantation experiments. *Tg:Pax7-CreERT2::R26^{mTmG}::Cripto^{loxP/-}* (*Cripto^{-cKO}*) and *Tg:Pax7-CreERT2::R26^{mTmG}* (Cripto^{-wt}) were generated by crossing Tg:Pax7-CreERT2::*Cripto*^{loxP/-} [24] with the reporter *R26^{mTmG}*, for *in vivo* and *ex vivo* studies of *Cripto* knockout. To achieve Satellite Cell (SCs) recombination, mice were injected intraperitoneally (IP) with Tamoxifen (Tmx; 60μg/g; Sigma-Aldrich) for 5 days consecutively. Mice were genotyped for recombination as described previously[24]. Primers used for genotyping are listed in Table S2.

Primary Satellite Cells isolation—Primary SCs were obtained from adult hind limb muscles after enzymatic digestion, followed by FACS-sorting at the time points indicated in figure legends. Total cells were isolated from quiescent or injured muscles at time points indicated in figure legends. Injury was performed by intramuscular (IM) injection of 10μM Cardiotoxin (CTX; Latoxan) in 6 muscles (20μl in each Tibialis Anterior, 30μl in each Gastrocnemius, 30μl in each Quadriceps of 10μM CTX). After dissection muscles were dissociated in digestion solution 3U/ml Dispase II (10887800 - Roche), 0,5U/ml Collagenase A (10103586001 - Roche), DNAse I (10μg/μl - 11284932001 - Roche), 400μM CaCl$_2$ and 5μM MgCl$_2$ in Phosphate Buffer Saline (PBS), for 90 minutes at 37°C, in a shaking bath. Following incubation, cells were washed with 0.2% of Bovine Serum Albumin (BSA - Sigma) in HBSS (Gibco) and filtered with 100 μm, 70 μm and 40μm strainers (Corning), sequentially.

Single myofibers isolation—Isolated myofibers were obtained from resting Extensor Digitorum Longus (EDL). Muscles were harvested from tendon to tendon and digested in a 37°C pre-heated solution 0.3% Collagenase (Sigma-Aldrich) and 1mM Pyruvate Sodium (Gibco) in Dulbecco's Modified Eagle's medium (DMEM; Gibco) without serum, for 1 hour at 37 ° C without shaking. After digestion muscles were transferred in horse serum -coated plates and filled with pre-heated solution of 1mM Pyruvate Sodium (Gibco), 1% Pen/Strep (Euroclone) in DMEM (gibco). Myofibers detaching from muscles were cleaned from debris by collecting them individually with a Fetal Bovine Serum (FBS; Euroclone) serum -coated pipette. All steps were performed on stereomicroscope (Leica).

Method details

Florescence Activated Cell Sorting (FACS)—After enzymatic digestion, cells were re-suspended in cell sorting buffer (PBS, 10% goat serum, 2mM EDTA). GFP positive cells were sorted by using the cell sorter FACS Aria II (BD Biosciences) and used for further analysis. Otherwise, cell bulks were blocked for 15 minutes in Hank's Balanced Salt Solution (HBSS; Gibco) supplemented with 0.2% BSA, incubated with anti–CRIPTO-APC (R&D, FAB1538) for 45 minutes at RT, and sorted by GFP expression and/or for CRIPTO expression levels. GFP positive population was gated by PerCp-Cy5–5A or SSC, as mock channel, and GFP. CRIPTO was plotted against GFP+ population by using the anti-CRIPTO-APC antibody. Isotype-matched control was used for setting the threshold. CRIPTO^{Pos} and CRIPTO^{Neg} cell fractions corresponded to ≈25% of the total GFP+ population. A sample of the sorted cells was re-analysed by FACS, ranging purity of the isolated from 80% to 100%. For each experiment, each mouse was analysed separately. All analyses and quantitation were performed using BD FACSDiva software.

Cytospin and immunofluorescence of FACS sorted cells—Cells were FACS-sorted into 20% FBS and cytocentrifuged at 800rpm for 8 minutes on SuperFrost Plus™ slides by using a Thermo Shandon Cytocentrifuge (Cytospin™ 4 Cytocentrifuge). Adhered cells were then fixed with 4% paraformaldehyde (PFA). Cells were blocked with 1% BSA in PBS for 30 minutes. Cells were permeabilized for intracellular stainings with 0.5% Triton X-100. Primary antibodies used were: CRIPTO (1:100, Cell Signaling), SNA biotinylated (1:8000, Vector Laboratories), P4HB (1:200, Abcam), PAX7 (1:5, Hybridoma Bank). After

washing cells were incubated with fluorophore-conjugated secondary antibodies, Alexa Fluor 488, 594 or streptavidin-Cy3 conjugated (1:600, Molecular Probes). Cell nuclei were counterstained with DAPI (Roche). Nikon ECLIPSE NI-E fluorescence microscope or confocal microscope Nikon A1 were used for image acquisition/elaboration.

In vitro repopulation and trafficking studies of FACS isolated cells—For repopulation studies cells were incubated at low serum (1% goat serum) for 1 hour and then re-stained or left untreated with the anti-CRIPTO-APC antibody (1 hour) and analyzed by FACS. For trafficking studies cells were incubated, immediately after sorting, at RT or 20°C with or without DMSO (Sigma-Aldrich), Nocodazole (33μM, Sigma-Aldrich), U73122 (1μM, Selleckchem), Varespladib (10nM, Selleckchem), FIPI (100nM, Selleckchem).

Intracellular staining on FACS isolated cells—Freshly isolated CRIPTO^{Pos} and CRIPTO^{Neg} cells were fixed with 2% (wt/vol) paraformaldehyde (PFA) before permeabilization with 0.2% Triton X-100 and staining with anti–CRIPTO-APC (R&D, FAB1538) and Rhodamine Phalloidin (ThermoFisher Scientific, code: R415). After treatments (≈1.5 hours) cells were analysed using BD FACSDiva software.

Cell cycle analysis—Injured skeletal muscles were collected at 3 days post-injury. CRIPTO$^{Pos/Neg}$ SCs from Pax7-nGFP mice, or recombinant SCs cells, were FACS-sorted in growth medium 20% FBS (Euroclone), 2% UltraSerum (LifeScience) and 1% Pen/Strep (EuroClone) in 40% DMEM (Euroclone) and 40% F-12 Nutrient Mixture - GlutaMAX (Gibco) and incubated 15 minutes at RT. Cells were then centrifuged 5 minutes at 2000rpm. Cell pellets were incubated in Sodium (Na)-Citrate buffer [0.1% Na-Citrate, 0.05% Nonidet P-40 (Sigma-Aldrich), 50μg/ml Propidium Iodide and 0.2μg/ml RNAse (Qiagen)] for 15 minutes and then analysed using a BD FACS Canto.

Mito Tracker analysis—For the estimation of active mitochondria CRIPTO$^{Pos/Neg}$ SCs were incubated, for 30 min at 37°C, with 100 nM of MitoTracker Orange CM-H2TMRos (546 nm; ThermoFisher Scientific, code: M7511) in HBSS (Gibco) supplemented with 0,2% BSA and the intensity fluorescence was measured using a BD FACS Canto.

Quantification of 5hmC—For 5-hydroxymethylCytosine (5hmC) quantification, sorted CRIPTO$^{Pos/Neg}$ SCs were collected and genomic DNA was extracted using the Wizard$^{®}$ Genomic DNA Purification kit (Promega). 5hmC levels were measured by ELISA-based assay, using the MethylFlashTM Global DNA Hydroxymethylation (5hmC) ELISA Easy Kit (Epigentek) and normalized to DNA content, according to manufacturer instructions. The absorbance was measured at 450 nm using the spectrophotometer Synergy H1 Microplate Reader (BioTek).

Quantitative RT-PCR—Total RNA was isolated in TRIzol (Sigma-Aldrich) by using the Direct-Zol Miniprep kit (Zimo-Research) following manufacturer's instructions, and reverse transcribed using QuantiTect Reverse Transcription Kit (Qiagen). Quantitative real-time PCR (qRT-PCR) was performed using SYBR Green PCR master mix (FluoCycle II^{TM} SYBR$^{®}$, EuroClone). Primers used are listed in Table S2.

RNA-seq analysis—CRIPTO[Pos] and CRIPTO[Neg] SCs were sorted from injured hind limb muscles of Tg:Pax7-nGFP mice, at 3 dpi. FACS-sorting was performed on cell sorter FACS Aria II (BD Biosciences). Pooled GFP[+]ASCs from 4 individual mice (M1, M2, M3, M4) were analysed by RNA-seq. Total RNA from sorted cells was extracted in TRIzol (Sigma-Aldrich), using Direct-Zol Miniprep kit (Zimo-Research) following the manufacturer's instructions. Stranded total RNA (2×20M) library was prepared for the Illumina NextSeq500 platform (TruSeq stranded total RNA with Ribo-Zero) and paired-end 2×75 cycles, ~40,000,000 reads/sample sequencing has been performed at https://www.genomix4life.com/it/. Fastq underwent Quality Control using FastQC tool (v0.11.3; http://www.bioinformatics.babraham.ac.uk/projects/fastqc/). Trimmomatic (v0.36; [55]) was used to remove low quality bases of the sequencing reads, with parameters: PE -phred33 HEADCROP:12.The mapping of paired-end reads was performed using STAR (v2.5.2a)[56] on reference genome assembly mm10 (GRCm38.81) from Ensembl [57], with parameters: --outSAMtype BAM SortedByCoordinate --outFilterMultimapNmax 20 --alignSJoverhangMin 8 -- alignSJDBoverhangMin 1 --outFilterMismatchNmax 999 --outFilterMismatchNoverReadLmax 0.04 - -alignIntronMin 20 --alignIntronMax 1000000 --alignMatesGapMax 1000000. The quantification of transcripts expressed for each sample was performed with HTSeq-Count (HTSeq v0.6.1p1;[58]), with parameters: -f bam -m union --order pos -s reverse. Counts data from all conditions were filtered based on their raw count, keeping only those where the sum of the counts for all samples was higher than 10, then normalised and logged with DESeq2 v1.20.0 rlog function[59]. DESeq2 was also used to perform Principal Component Analysis (PCA) and differential gene expression analysis (significance threshold: FDR<0.05). DAVID Functional Annotation Tool 6.8 (https://david.ncifcrf.gov/summary.jsp) and GSEA v3.0 (https://www.gsea-msigdb.org/gsea/index.jsp;[60]) were used for GO analysis of differentially expressed genes.

Immunofluorescence on plated cells—Sorted cells were cultured at low density (3500cells/cm^2) in Matrigel (BD) -coated plates in in growth medium 20% FBS (Euroclone), 2% UltraSerum (LifeScience) and 1% Pen/Strep (EuroClone) in 40% DMEM (Euroclone) and 40% F-12 Nutrient Mixture - GlutaMAX (Gibco). Cells were fixed for 10 minutes with 4% (wt/vol) paraformaldehyde (PFA) in PBS and blocked with 1% BSA in PBS for 30 minutes at RT. Primary antibodies used were: MYOD (1:50, Santa Cruz), GFP (1:800, Abcam), PAX7 (1:5, Hybridoma Bank), KI67 (1:100, Monosan), MYOG (1:5, Hybridoma Bank). After washing cells were incubated with fluorophore-conjugated secondary antibodies, Alexa Fluor 488 or 594 (1:600, Molecular Probes). Cell nuclei were counterstained with DAPI (Roche). Dmi6000B (Leica) or ECLIPSE NI-E (Nikon) fluorescence microscopes were used for image acquisition/elaboration.

Time lapse imaging—SCs were isolated from injured hind limb muscles of three Tg:Pax7-nGFP *mice*, at 3 dpi and CRIPTO[Pos] and CRIPTO[Neg] cells were FACS-sorted into Matrigel-coated 96-well plates in quadruplicate (3000cells/cm^2). Time-lapse microscopy was performed over a period of 20 hours and images were captured every 10 minutes using Dmi6000B microscope (Leica) with a DFC420 camera (OKOLAB cage). Mitotic duration was analyzed using time-lapse microscopy videos and defined as the difference between the mitotic entry frame (round shape formation) and the first frame of cytokinesis (visualization

of two individual cells). Data from the three individual experiments was pooled and used to calculate the mean event duration.

Cell trajectories were reconstructed from time-lapse videos using the command "manual tracking" of Fiji Software using a "local barycentre" centring correction evaluated in a 20-pixel square region of interest. Cells undergoing division or exhibiting extended contacts with other cells were not considered in the tracking process. The cell root-mean-square speed (S) and persistence time (P) were derived from a persistence random walk model as described by Dickinson and Tranquillo[61]. Briefly, the Mean Square Displacement (MSD) as a function of the time interval t of each cell's centroid was calculated according to the overlapping time intervals method. Then the MSD was averaged over the cell population. Finally, S and P were derived from a non-linear fit to the equation:

$$\left\langle d^2 \right\rangle_t = S^2 P^2 \left[t - P \left(1 - e^{-t/P} \right) \right].$$

The operator denotes the average over time intervals and over the cell population. As the population pooled MSD is very scattered at long time intervals owing to the small number of data point available, the nonlinear fit was performed in the 0 to ~300 minutes time interval.

Immunofluorescence and EdU incorporation on isolated myofibers—For cell proliferation studies, floating myofibers were incubated with 5μM EdU (Invitrogen). Myofibers were collected and processed, after fixation, for immunostaining with antibodies anti-GFP (1:800, Abcam) and -phospho p38 (1:50, Cell Signalling) or Click-iT EdU Alexa Fluor 647 imaging kit (Invitrogen) according to the manufacturer's instructions. After washing cells were incubated with fluorophore-conjugated secondary antibodies, Alexa Fluor 488 or 594 (1:600, Molecular Probes). Cell nuclei were counterstained with DAPI (Roche). Image acquisition/elaboration were performed by using Nikon A1 confocal microscope or Nikon ECLIPSE NI-E fluorescence microscope.

Muscle regeneration and EdU, BrdU delivery—Tmx-treated mice were injected IM in TA muscles with 20μl of 10uM CTX and muscles were collected at time points indicated in figure legends. BrdU [50μg/gram body weight (gr), Sigma-Aldrich] were injected IP after CTX injection for 5 or 10 days consecutively. EdU (20μg/gr, Invitrogen) were injected IP 24 and 2 hours before sacrifice.

Intramuscular transplantation of FACS isolated satellite cells—Engraftment was performed as previously described[62]. Briefly, CRIPTO$^{Pos/Neg}$ derived from muscles of Pax7nGFP or Pax7nGFP::R26^{mTmG} mice and GFP+ cells derived from tmx-treated Tg:Pax7-CreERT2::R26mTmG::*Cripto$^{loxP/-}$* (*Cripto^{-cKO}*) and Tg:Pax7-CreERT2::R26^{mTmG} (*Cripto^{-wt}*) mice were FACS-isolated at 3 dpi and injected into TA muscles of C57BL/6 recipient mice, that were CTX-injured 24 hours before transplantation. The number of injected cells was 20000 per TA muscle. After four weeks, transplanted muscles were re-injured for further FACS-analysis or isolated and frozen in isopentane cooled with liquid nitrogen.

Tissue preparation and histological analysis—Collected muscles were prepared for following analysis as previously described[24]. Briefly, tissues were snap-frozen in liquid nitrogen-cooled isopentane. Sections (10μm-thick) were stained with Hematoxylin & Eosin (H&E). Images were captured on DM6000B (Leica) and analyses were performed using ImageJ software[63].

Immunofluorescence on sections—Muscle sections were processed as previously described[64]. Briefly, cryosections were fixed in 4% (wt/vol) PFA and permeabilized in ice-cold methanol for 6 minutes at −20°C. Slides were, then, subjected to antigen retrieval in boiling 10mM Na-Citrate (pH 6.0) -solution for 15 minutes, followed by cooling in the same solution for 30 minutes. Sections were then incubated in blocking buffer [4% IgG-free BSA (Jackson) in PBS] for 2 hours and endogenous immunoglobulins were blocked with AffiniPure Fab Fragment goat anti-mouse IgG (Jackson) for 30 minutes at RT. Primary antibodies were used as follows: anti -BrdU (1:50, GeneTex), -PAX7 (1:10, Developmental Studies Hybridoma Bank) and -KI67 (1:50, ThermoFisher) and -GFP (1:800, Abcam). For EdU detection, sections were subjected to the Click-iT EdU reaction (Invitrogen, Alexa Fluor A647 azide) according to manufacturer's instructions. Antibody binding was visualized by using fluorophore-conjugated secondary antibodies Alexa Fluor (1:600, Invitrogen) or biotin-conjugated goat anti-mouse (1:600, Jackson) and Cy3- (Jackson) or −488 and −647 (Invitrogen) conjugated streptavidin for PAX7 visualization. For analysis of GFP expression, slides were examined under a microscope and GFP positive fibers were scored only when detected on the fluorescein filter and not on the rhodamine filter. Nuclei were counterstained with DAPI (Roche) and FluoSave Reagent (Calbiochem) was used for mounting. Labelling was visualized and images were acquired by using a DM6000B (Leica) or ECLIPSE NI-E (Nikon) microscopes.

Quantification and statistical analysis

Experiments were all performed with a minimum of three biological samples. Replicate number is indicated in figure legends as $n=$. Results are presented as the mean ± SEM (Standard Error of the Mean) or median. To determine significance between two groups, comparisons were made using unpaired Student t-tests or Mann-Whitney-Wilcoxon test. *p 0.05, **p 0.005, ***p 0.0005, and ****p 0.0005 were considered statistically significant.

Supplementary Material

Refer to Web version on PubMed Central for supplementary material.

Acknowledgments

References

1. Rocheteau P, Gayraud-Morel B, Siegl-Cachedenier I, Blasco MA, and Tajbakhsh S. (2012). A Subpopulation of Adult Skeletal Muscle Stem Cells Retains All Template DNA Strands after Cell Division. Cell 148, 112–125. 10.1016/j.cell.2011.11.049. [PubMed: 22265406]

2. Kuang S, Kuroda K, Le Grand F, and Rudnicki MA (2007). Asymmetric Self-Renewal and Commitment of Satellite Stem Cells in Muscle. Cell 129, 999–1010. 10.1016/j.cell.2007.03.044. [PubMed: 17540178]

3. Ono Y, Masuda S, Nam HS, Benezra R, Miyagoe-Suzuki Y, and Takeda S. (2012). Slow-dividing satellite cells retain long-term self-renewal ability in adult muscle. J Cell Sci 125, 1309–1317. 10.1242/jcs.096198. [PubMed: 22349695]

4. Dell'Orso S, Juan AH, Ko KD, Naz F, Perovanovic J, Gutierrez-Cruz G, Feng X, and Sartorelli V. (2019). Single cell analysis of adult mouse skeletal muscle stem cells in homeostatic and regenerative conditions. Development 146. 10.1242/dev.174177.

5. Scaramozza A, Park D, Kollu S, Beerman I, Sun X, Rossi DJ, Lin CP, Scadden DT, Crist C, and Brack AS (2019). Lineage Tracing Reveals a Subset of Reserve Muscle Stem Cells Capable of Clonal Expansion under Stress. Cell Stem Cell 24, 944–957 e5. 10.1016/j.stem.2019.03.020. [PubMed: 31006621]

6. Yin H, Price F, and Rudnicki MA (2013). Satellite Cells and the Muscle Stem Cell Niche. Physiological Reviews 93, 23–67. 10.1152/physrev.00043.2011. [PubMed: 23303905]

7. Schmidt M, Schüler SC, Hüttner SS, von Eyss B, and von Maltzahn J. (2019). Adult stem cells at work: regenerating skeletal muscle. Cell. Mol. Life Sci. 76, 2559–2570. 10.1007/s00018-019-03093-6. [PubMed: 30976839]

8. Sousa-Victor P, García-Prat L, and Muñoz-Cánoves P. (2022). Control of satellite cell function in muscle regeneration and its disruption in ageing. Nat Rev Mol Cell Biol 23, 204–226. 10.1038/s41580-021-00421-2. [PubMed: 34663964]

9. Rue P, and Martinez Arias A. (2015). Cell dynamics and gene expression control in tissue homeostasis and development. Mol Syst Biol 11, 792. 10.15252/msb.20145549. [PubMed: 25716053]

10. Snippert HJ, van der Flier LG, Sato T, van Es JH, van den Born M, Kroon-Veenboer C, Barker N, Klein AM, van Rheenen J, Simons BD, et al. (2010). Intestinal crypt homeostasis results from neutral competition between symmetrically dividing Lgr5 stem cells. Cell 143, 134–144. 10.1016/j.cell.2010.09.016. [PubMed: 20887898]

11. Simons BD, and Clevers H. (2011). Strategies for homeostatic stem cell self-renewal in adult tissues. Cell 145, 851–862. 10.1016/j.cell.2011.05.033. [PubMed: 21663791]

12. Porpiglia E, Mai T, Kraft P, Holbrook CA, de Morree A, Gonzalez VD, Hilgendorf KI, Frésard L, Trejo A, et al. (2022). Elevated CD47 is a hallmark of dysfunctional aged muscle stem cells that can be targeted to augment regeneration. Cell Stem Cell 29, 1653–1668.e8. 10.1016/j.stem.2022.10.009. [PubMed: 36384141]

13. Eliazer S, Sun X, Barruet E, and Brack AS (2022). Heterogeneous levels of delta-like 4 within a multinucleated niche cell maintains muscle stem cell diversity. eLife. 10.7554/eLife.68180.

14. Evano B, Khalilian S, Le Carrou G, Almouzni G, and Tajbakhsh S. (2020). Dynamics of Asymmetric and Symmetric Divisions of Muscle Stem Cells In Vivo and on Artificial Niches (2020). Cell Reports 30, 3195–3206.e7. 10.1016/j.celrep.2020.01.097. [PubMed: 32160529]

15. Gessain G, Bleriot C, and Ginhoux F. (2020). Non-genetic Heterogeneity of Macrophages in Diseases-A Medical Perspective. Front Cell Dev Biol 8, 613116. 10.3389/fcell.2020.613116. [PubMed: 33381508]

16. Barzgar Barough N, Sajjadian F, Jalilzadeh N, Shafaei H, and Velaei K. (2021). Understanding breast cancer heterogeneity through non-genetic heterogeneity. Breast Cancer 28, 777–791. 10.1007/s12282-021-01237-w. [PubMed: 33723745]

17. Giuliani G, Vumbaca S, Fuoco C, Gargioli C, Giorda E, Massacci G, Palma A, Reggio A, Riccio F, Rosina M, et al. (2021). SCA-1 micro-heterogeneity in the fate decision of dystrophic fibro/adipogenic progenitors. Cell Death Dis 12, 122. 10.1038/s41419-021-03408-1. [PubMed: 33495447]

18. Capp JP, Jolly MK, and Sharma A. (2021). Editorial: Non-Genetic Heterogeneity in Development and Disease. Front Genet 12, 731814. 10.3389/fgene.2021.731814. [PubMed: 34434224]

19. Loewer A. and Lahav G. (2011). We are all individuals: causes and consequences of non-genetic heterogeneity in mammalian cells. Current Opinion in Genetics & Development 21, 753–758. 10.1016/j.gde.2011.09.010. [PubMed: 22005655]

20. Huang S. (2009). Non-genetic heterogeneity of cells in development: more than just noise. Development 136, 3853–3862. 10.1242/dev.035139. [PubMed: 19906852]

21. Schmitz J, Noll T, and Grünberger A. (2019). Heterogeneity Studies of Mammalian Cells for Bioproduction: From Tools to Application. Trends in Biotechnology 37, 645–660. 10.1016/j.tibtech.2018.11.007. [PubMed: 30642642]

22. Huang S. (2011). Systems biology of stem cells: three useful perspectives to help overcome the paradigm of linear pathways. Philos Trans R Soc Lond B Biol Sci 366, 2247–2259. 10.1098/rstb.2011.0008. [PubMed: 21727130]

23. Puri PL (2022). A post-middle-age crisis for CD47 and THBS1 that turns into a vicious cycle. Cell Stem Cell 29, 1613–1615. 10.1016/j.stem.2022.11.003. [PubMed: 36459961]

24. Guardiola O, Lafuste P, Brunelli S, Iaconis S, Touvier T, Mourikis P, De Bock K, Lonardo E, Andolfi G, Bouché A, et al. (2012). Cripto regulates skeletal muscle regeneration and modulates satellite cell determination by antagonizing myostatin. Proc. Natl. Acad. Sci. U.S.A. 109. 10.1073/pnas.1204017109.

25. Prezioso C, Iaconis S, Andolfi G, Zentilin L, Iavarone F, Guardiola O, and Minchiotti G. (2015). Conditional Cripto overexpression in satellite cells promotes myogenic commitment and enhances early regeneration. Front Cell Dev Biol 3, 31. 10.3389/fcell.2015.00031. [PubMed: 26052513]

26. Fiorenzano A, Pascale E, D'Aniello C, Acampora D, Bassalert C, Russo F, Andolfi G, Biffoni M, Francescangeli F, Zeuner A, et al. (2016). Cripto is essential to capture mouse epiblast stem cell and human embryonic stem cell pluripotency. Nat Commun 7, 12589. 10.1038/ncomms12589. [PubMed: 27586544]

27. Francescangeli F, Contavalli P, De Angelis ML, Baiocchi M, Gambara G, Pagliuca A, Fiorenzano A, Prezioso C, Boe A, Todaro M, et al. (2015). Dynamic regulation of the cancer stem cell compartment by Cripto-1 in colorectal cancer. Cell Death Differ 22, 1700–1713. 10.1038/cdd.2015.19. [PubMed: 26343543]

28. Francescangeli F, De Angelis ML, Rossi R, Sette G, Eramo A, Boe A, Guardiola O, Tang T, Yu S, Minchiotti G, Zeuner A. (2022). CRIPTO Is a Marker of Chemotherapy-Induced Stem Cell Expansion in Non-Small Cell Lung Cancer. Frontiers in oncology 12. 10.3389/fonc.2022.830873.

29. Sambasivan R, Gayraud-Morel B, Dumas G, Cimper C, Paisant S, Kelly RG, and Tajbakhsh S. (2009). Distinct regulatory cascades govern extraocular and pharyngeal arch muscle progenitor cell fates. Dev Cell 16, 810–821. 10.1016/j.devcel.2009.05.008. [PubMed: 19531352]

30. Oprescu SN, Yue F, Qiu J, Brito LF, and Kuang S. (2020). Temporal Dynamics and Heterogeneity of Cell Populations during Skeletal Muscle Regeneration. iScience 23, 100993. 10.1016/j.isci.2020.100993. [PubMed: 32248062]

31. Fukada S, Higashimoto T, and Kaneshige A. (2022). Differences in muscle satellite cell dynamics during muscle hypertrophy and regeneration. Skeletal Muscle 12, 1–10. 10.1186/s13395-022-00300-0. [PubMed: 35039091]

32. Chang HH, Hemberg M, Barahona M, Ingber DE, and Huang S. (2008). Transcriptome-wide noise controls lineage choice in mammalian progenitor cells. Nature 453, 544–547. 10.1038/nature06965. [PubMed: 18497826]

33. Ramirez J-M, Bai Q, Péquignot M, Becker F, Kassambara A, Bouin A, Kalatzis V, Dijon-Grinand M, and De Vos J. (2013). Side scatter intensity is highly heterogeneous in undifferentiated pluripotent stem cells and predicts clonogenic self-renewal. Stem Cells Dev 22, 1851–1860. 10.1089/scd.2012.0658. [PubMed: 23360234]

34. Dumont NA, Wang YX, von Maltzahn J, Pasut A, Bentzinger CF, Brun CE, and Rudnicki MA (2015). Dystrophin expression in muscle stem cells regulates their polarity and asymmetric division. Nat Med 21, 1455–1463. 10.1038/nm.3990. [PubMed: 26569381]

35. Ecsedi S, Rodríguez-Aguilera J, and Hernandez-Vargas H. (2018). 5-Hydroxymethylcytosine (5hmC), or How to Identify Your Favorite Cell. Epigenomes 2, 3. 10.3390/epigenomes2010003.

36. Evano B, and Tajbakhsh S. (2018). Skeletal muscle stem cells in comfort and stress. NPJ Regen Med 3, 24. 10.1038/s41536-018-0062-3.

37. Taubenberger AV, Baum B, and Matthews HK (2020). The Mechanics of Mitotic Cell Rounding. Front Cell Dev Biol 8, 687. 10.3389/fcell.2020.00687. [PubMed: 32850812]

38. Thery M, and Bornens M. (2008). Get round and stiff for mitosis. HFSP J 2, 65–71. 10.2976/1.2895661. [PubMed: 19404473]

39. Muzumdar MD, Tasic B, Miyamichi K, Li L, and Luo L. (2007). A global double-fluorescent Cre reporter mouse. Genesis 45, 593–605. 10.1002/dvg.20335. [PubMed: 17868096]

40. Blanchet M-H, Le Good JA, Oorschot V, Baflast S, Minchiotti G, Klumperman J, and Constam DB (2008). Cripto Localizes Nodal at the Limiting Membrane of Early Endosomes. Sci. Signal. 1. 10.1126/scisignal.1165027.

41. Constam DB (2009). Riding shotgun: a dual role for the epidermal growth factor-Cripto/FRL-1/Cryptic protein Cripto in Nodal trafficking. Traffic 10, 783–791. 10.1111/j.1600-0854.2009.00874.x. [PubMed: 19302412]

42. Minchiotti G, Parisi S, Liguori G, Signore M, Lania G, Adamson ED, Lago CT, and Persico MG (2000). Membrane-anchorage of Cripto protein by glycosylphosphatidylinositol and its distribution during early mouse development. Mech Dev 90, 133–142. 10.1016/s0925-4773(99)00235-x. [PubMed: 10640699]

43. Watanabe K, Bianco C, Strizzi L, Hamada S, Mancino M, Bailly V, Mo W, Wen D, Miatkowski K, Gonzales M, et al. (2007). Growth factor induction of Cripto-1 shedding by glycosylphosphatidylinositol-phospholipase D and enhancement of endothelial cell migration. J Biol Chem 282, 31643–31655. 10.1074/jbc.M702713200. [PubMed: 17720976]

44. Lee G-H, Fujita M, Takaoka K, Murakami Y, Fujihara Y, Kanzawa N, Murakami K, Kajikawa E, Takada Y, Saito K, et al. (2016). A GPI processing phospholipase A2, PGAP6, modulates Nodal signaling in embryos by shedding CRIPTO. The Journal of Cell Biology 215, 705. 10.1083/jcb.201605121. [PubMed: 27881714]

45. Rigo A, and Vinante F. (2017). Flow cytometry analysis of receptor internalization/shedding. Cytometry Part B: Clinical Cytometry 92, 291–298. 10.1002/cyto.b.21392. [PubMed: 27342211]

46. Kuismanen E, and Saraste J. (1989). Low temperature-induced transport blocks as tools to manipulate membrane traffic. Methods Cell Biol 32, 257–274. 10.1016/s0091-679x(08)61174-7. [PubMed: 2691852]

47. Schmoranzer J, Kreitzer G, and Simon SM (2003). Migrating fibroblasts perform polarized, microtubule-dependent exocytosis towards the leading edge. J Cell Sci 116, 4513–4519. 10.1242/jcs.00748. [PubMed: 14576345]

48. Troy A, Cadwallader AB, Fedorov Y, Tyner K, Tanaka KK, and Olwin BB (2012). Coordination of Satellite Cell Activation and Self-Renewal by Par-Complex-Dependent Asymmetric Activation of p38α/β MAPK. Cell Stem Cell 11, 541–553. 10.1016/j.stem.2012.05.025. [PubMed: 23040480]

49. Chakkalakal JV, Christensen J, Xiang W, Tierney MT, Boscolo FS, Sacco A, and Brack AS (2014). Early forming label-retaining muscle stem cells require p27kip1 for maintenance of the primitive state. Development 141, 1649–1659. 10.1242/dev.100842. [PubMed: 24715455]

50. Dentice M, Biressi S, Giordani L, and Guardiola O. (2023). Editorial: Cellular heterogeneity in physiological and pathological myogenesis. Front. Cell Dev. Biol. 11, 1235520. 10.3389/fcell.2023.1235520. [PubMed: 37397248]

51. Waldemer-Streyer RJ, Kim D, and Chen J. (2022). Muscle cell-derived cytokines in skeletal muscle regeneration. The FEBS Journal. 10.1111/febs.16372.

52. Gatenby RA (2019). The Role of Cell Membrane Information Reception, Processing, and Communication in the Structure and Function of Multicellular Tissue. International Journal of Molecular Sciences 20, 3609. 10.3390/ijms20153609. [PubMed: 31344783]

53. Randolph ME, and Pavlath GK (2015). A muscle stem cell for every muscle: variability of satellite cell biology among different muscle groups. Front. Aging Neurosci. 7. 10.3389/fnagi.2015.00190.

54. Taglietti V., Kefi K., Rivera L., Bergiers O., Cardone N., Coulpier F., Gioftsidi S,B, Drayton-Libotte B, Hou C, Authier F, et al. . (2023). Thyroid-stimulating hormone receptor signaling restores skeletal muscle stem cell regeneration in rats with muscular dystrophy. Science translational medicine 15. 10.1126/scitranslmed.add5275.

55. Bolger AM, Lohse M, and Usadel B. (2014). Trimmomatic: a flexible trimmer for Illumina sequence data. Bioinformatics 30, 2114–2120. 10.1093/bioinformatics/btu170. [PubMed: 24695404]

56. Dobin A, Davis CA, Schlesinger F, Drenkow J, Zaleski C, Jha S, Batut P, Chaisson M, and Gingeras TR (2013). STAR: ultrafast universal RNA-seq aligner. Bioinformatics 29, 15–21. 10.1093/bioinformatics/bts635. [PubMed: 23104886]

57. Hubbard T, Barker D, Birney E, Cameron G, Chen Y, Clark L, Cox T, Cuff J, Curwen V, Down T, et al. (2002). The Ensembl genome database project. Nucleic Acids Res 30, 38–41. 10.1093/nar/30.1.38. [PubMed: 11752248]

58. Anders S, Pyl PT, and Huber W. (2015). HTSeq--a Python framework to work with high-throughput sequencing data. Bioinformatics 31, 166–169. 10.1093/bioinformatics/btu638. [PubMed: 25260700]

59. Love MI, Huber W, and Anders S. (2014). Moderated estimation of fold change and dispersion for RNA-seq data with DESeq2. Genome Biol 15, 550. 10.1186/s13059-014-0550-8. [PubMed: 25516281]

60. Subramanian A, Tamayo P, Mootha VK, Mukherjee S, Ebert BL, Gillette MA, Paulovich A, Pomeroy SL, Golub TR, Lander ES, et al. (2005). Gene set enrichment analysis: A knowledge-based approach for interpreting genome-wide expression profiles. Proceedings of the National Academy of Sciences 102, 15545–15550. 10.1073/pnas.0506580102.

61. Dickinson RB, and Tranquillo RT (1993). A stochastic model for adhesion-mediated cell random motility and haptotaxis. J Math Biol 31, 563–600. [PubMed: 8376918]

62. Tierney M, and Sacco A. (2017). Engraftment of FACS Isolated Muscle Stem Cells into Injured Skeletal Muscle. Methods Mol Biol 1556, 223–236. 10.1007/978-1-4939-6771-1_11. [PubMed: 28247352]

63. Schneider CA, Rasband WS, and Eliceiri KW (2012). NIH Image to ImageJ: 25 years of image analysis. Nature methods 9. 10.1038/nmeth.2089.

64. Nicolas N, Marazzi G, Kelley K, and Sassoon D. (2005). Embryonic deregulation of muscle stress signaling pathways leads to altered postnatal stem cell behavior and a failure in postnatal muscle growth. Dev Biol 281, 171–183. 10.1016/j.ydbio.2005.02.022. [PubMed: 15893971]

Author Manuscript

Author Manuscript

Author Manuscript

Author Manuscript

Highlights

- Activated Satellite Cells (ASCs) show micro-heterogeneity of surface CRIPTO protein

- CRIPTO micro-heterogeneity identifies phenotypic and molecular variants within ASCs

- Fluctuation of surface CRIPTO preserves ASC self-renewal/differentiation equilibrium

- CRIPTO micro-heterogeneity secures ASC adaptive response to microenvironmental cues
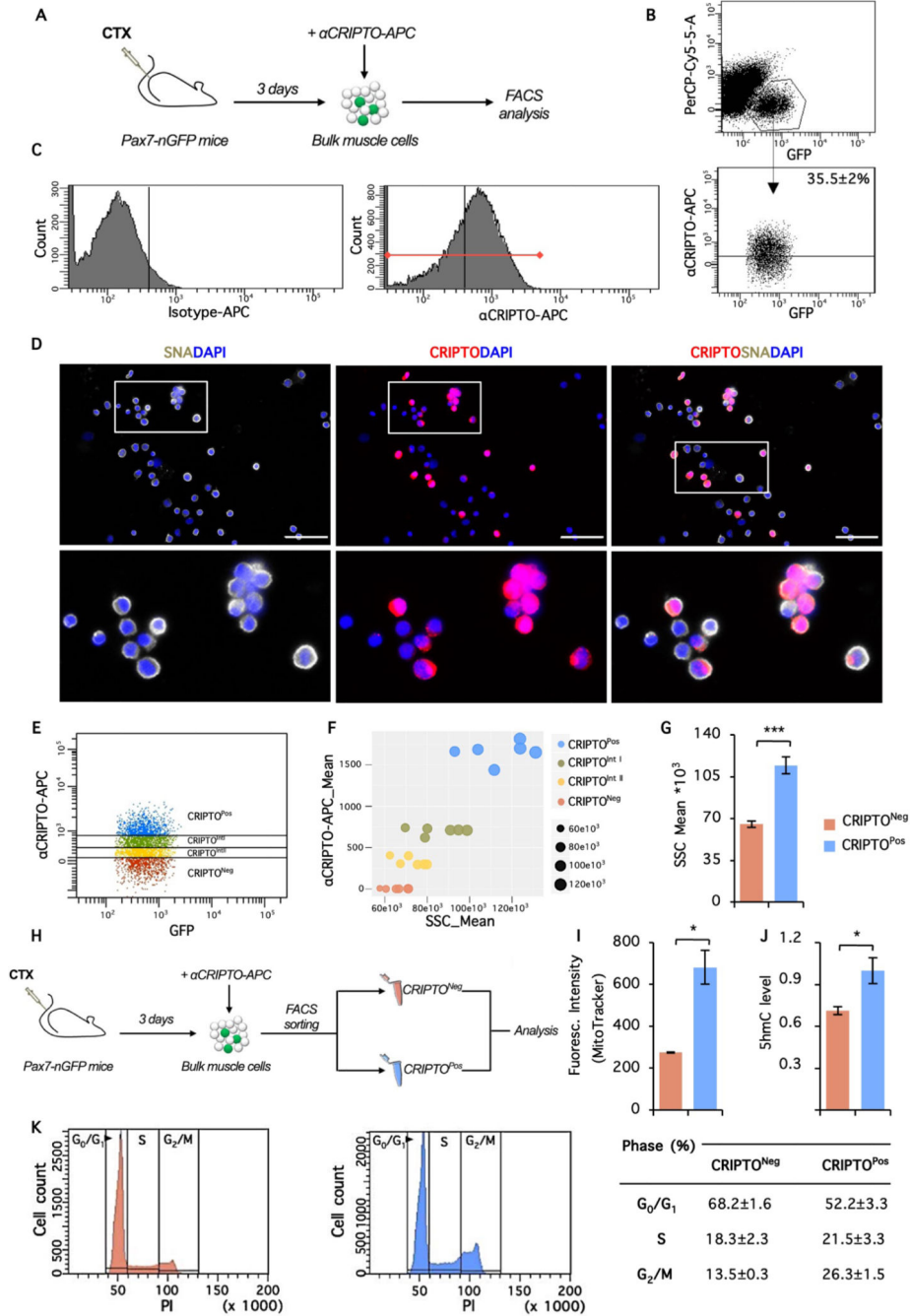
Figure 1. CRIPTO micro-heterogeneity in activated satellite cell (ASC) population. See also Figure S1

(**A**) Schematic representation of the experimental design. (**B**) Representative FACS plots showing the gating strategy. The percentage of CRIPTO-positive cells above the threshold is indicated (bottom panel). (**C**) Representative flow cytometry histograms showing surface CRIPTO micro-heterogeneity. Isotype-matched control was included to set the antibody threshold. (**D**) Representative images of CRIPTO (red) and Sambucus Nigra Lectin (SNA, white) staining on isolated/cytospun GFP+ASCs. Nuclei were counter-stained with DAPI.

Scale bar: 100μm. Higher magnification (5x) of the boxed area is shown (bottom panels). The images were pseudocolored-coded. (**E**) Representative dot plot showing the continuum of CRIPTO expression in GFP+ASC population. The colours represent different cell fraction based on CRIPTO fluorescence intensity. Each fraction corresponds to ~25-% of the GFP+population. (**F**) Scatter plot showing the relationship between Side Scatter mean values (SSC Mean) and Mean Fluorescence Intensity of *a*CRIPTO-APC antibody (*a*CRIPTO-APC_Mean)/cell fraction/mice. (**G**) Histogram showing the SSC_Mean of CRIPTO[Neg] and CRIPTO[Pos] cell fractions. (**H**) Schematic representation of the experimental design. (**I**) Mitotracker fluorescence intensity of CRIPTO[Neg] and CRIPTO[Pos] cells (*n*=4). (**J**) ELISA-based quantification of 5hmC levels. Data represent fold change *vs* CRIPTO[Pos] (*n*=4). (**K**) Representative flow cytometry histograms (left and middle) and quantification (right) of cell cycle distribution in CRIPTO[Neg] and CRIPTO[Pos] cells (*n*=4). Data represent mean ± SEM. *p < 0.05; ***p < 0.0005.
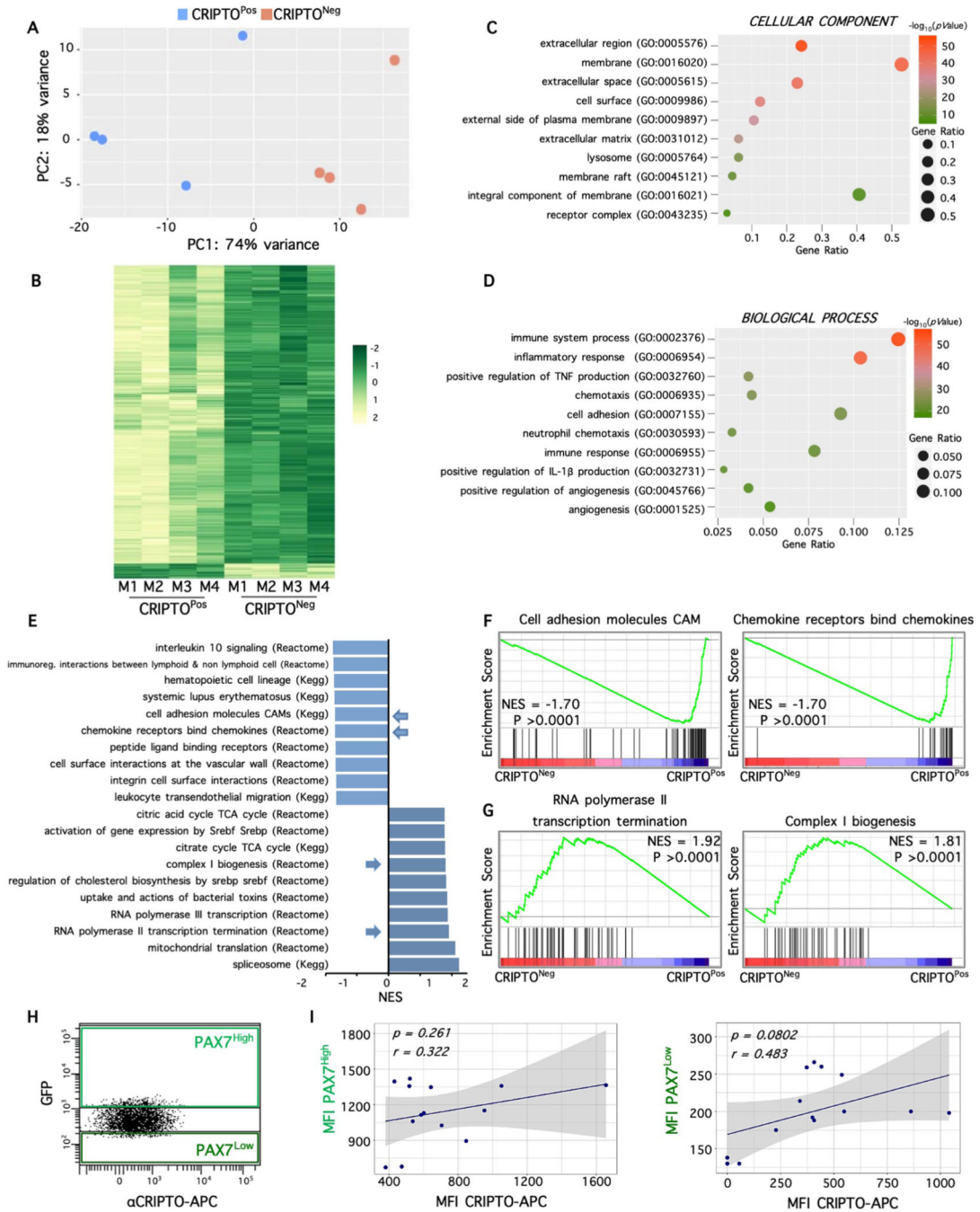
Figure 2. Transcriptional profiles of CRIPTO^Neg and CRIPTO^Pos cells and correlation between CRIPTO and PAX7 expression levels. See also Figure S2 and Table S1

(**A**) Principal component (PC) analysis of CRIPTO^Neg and CRIPTO^Pos cells. Each dot represents individual mice. (**B**) Heatmap of the differential gene expression genes from individual mice (M1-M4). The colour scale represents the normalized expression values of each gene. (**C-D**) Scatter plots representing statistically enriched Gene Ontology terms in Cellular Component (**C**) and Biological Process (**D**) categories. (**E**) Bar plot depicting the normalized enrichment scores (NES) of the top 10 most negatively and positively enriched

gene sets in CRIPTO[Neg] cells. (**F-G**) Selected GSEA-enrichment plots of negatively (**F**) and positively (**G**) enriched gene sets in CRIPTO[Neg] cells. (**H**) Representative dot plot showing the gating strategy for linear correlation analysis between the Mean Fluorescence Intensity (MFI) values of CRIPTO and GFP in the PAX7[High] and PAX7[Low] subpopulations. The gating strategy is based on PAX7 (GFP) expression levels (y-axis). Each cell fraction represents ~10-% of the GFP+ population. (**I**) Linear correlation analysis of the MFI of CRIPTO and GFP in the PAX7[High] (left panel) and PAX7[Low] (right panel) subpopulations from individual mice. The Pearson correlation coefficient (r) and its significance (p-value) are indicated.
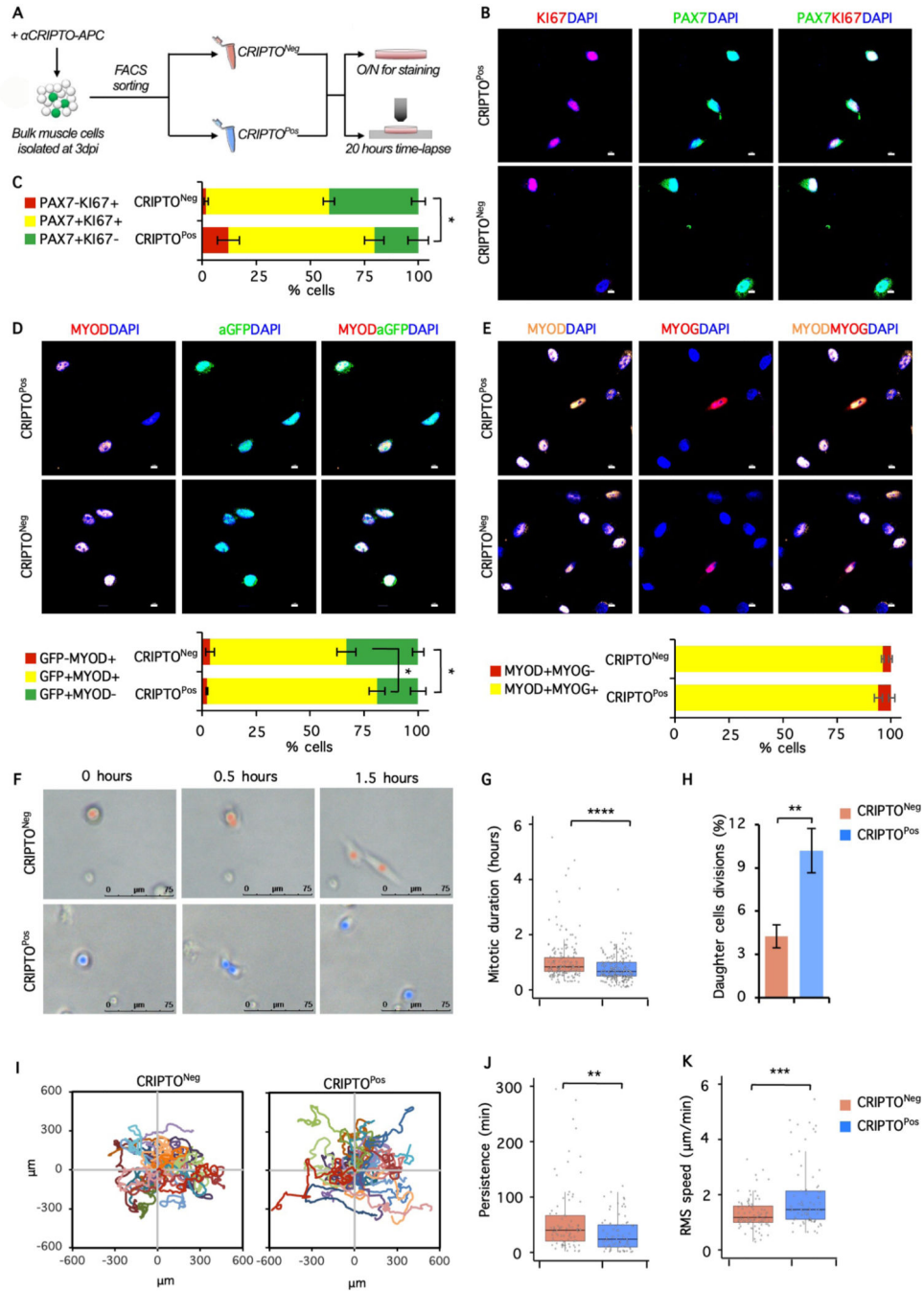
Figure 3. *In vitro* behavioural features of CRIPTO[Neg] and CRIPTO[Pos] cells. See also Videos S1 and S2.

(**A**) Schematic representation of the experimental design. GFP positive CRIPTO[Neg] and CRIPTO[Pos] ASCs were plated in growth medium (3000 cells/cm^{2}) for downstream analysis. (**B-C**) Representative images (**B**) of KI67 (red) and PAX7 (green) staining and quantification (**C**) of PAX7±/KI67± cells. (**D**) Representative images (upper panel) of MYOD (red) and GFP (green) staining and quantification (bottom panel) of GFP±/MYOD± cells. (**E**) Representative images (upper panel) of MYOD (orange) and MYOG (red) staining

and quantification (bottom panel) of GFP±/MYOD± cells. Nuclei were counter-stained with DAPI. Scale bar: 5μm. (**F**) Selected frames from time-lapse video microscopy of CRIPTO^{Neg} and CRIPTO^{Pos} cells. Scale bar: 75μm. (**G**) Box plot illustrating the distribution of mitotic duration events from pooled data of three individual experiments (CRIPTO^{Neg} =170 cells, CRIPTO^{Pos} n=202 cells). (**H**) Percentage of daughter cells undergoing second round of cell division. (**I**) Representative individual cell trajectory plots of CRIPTO^{Neg} and CRIPTO^{Pos} cells (25 cells/group). (**J-K**) Persistence time (**J**) and velocity [root mean square speed (RMS); **K**] of CRIPTO^{Neg} and CRIPTO^{Pos} cells from pooled data of three individual experiments (CRIPTO^{Neg} n=86 cells, CRIPTO^{Pos} n=75 cells). Data represent mean ± SEM. *p 0.05; **p 0.005; ***p 0.0005; ****p 0.00005.
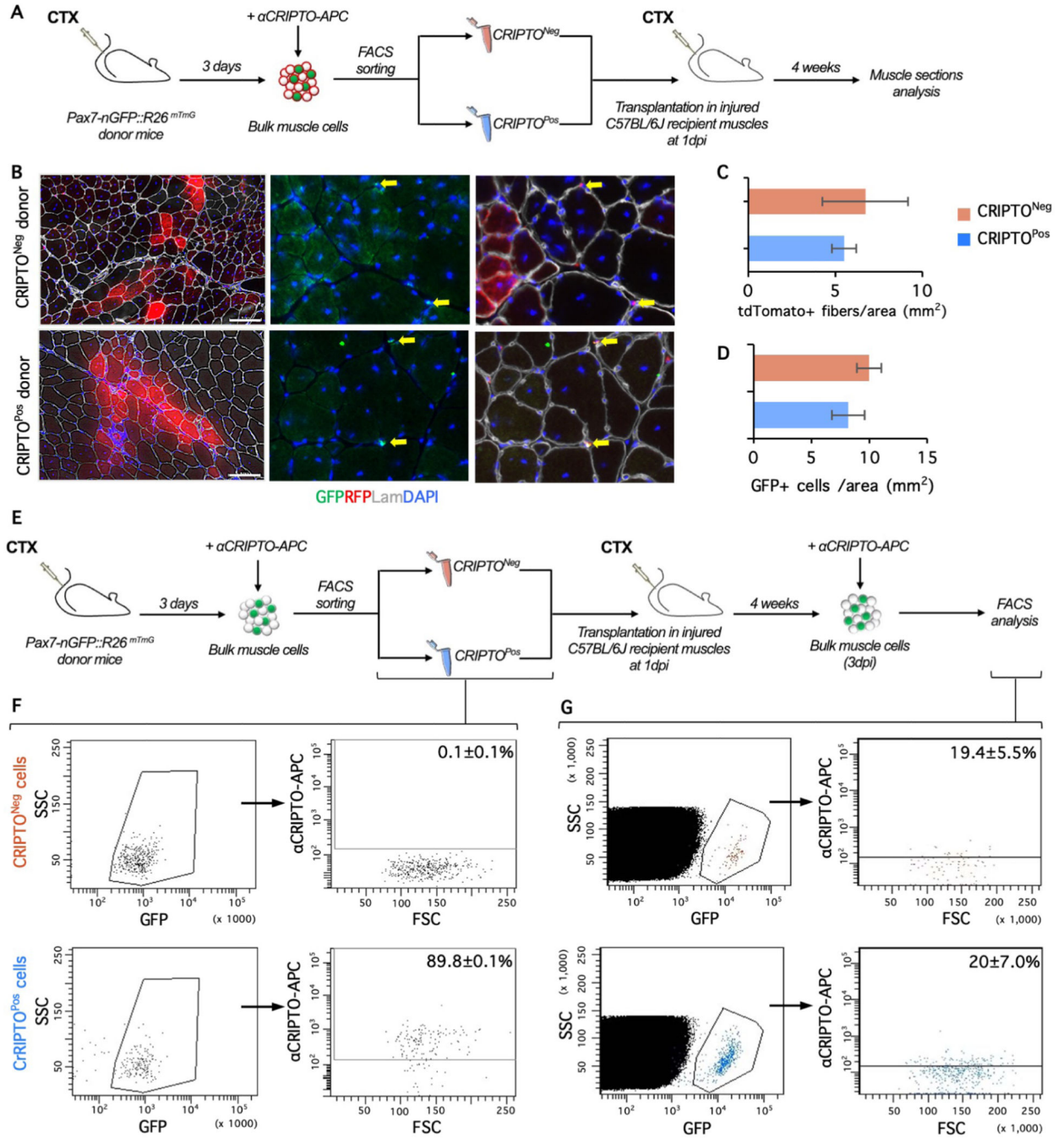
Figure 4. Regenerative potential of CRIPTO^Neg and CRIPTO^Pos cells and reconstitution of naïve CRIPTO micro-heterogeneity following *in vivo* cell transplantation.

(**A**) Schematic representation of the experimental design. (**B**) Representative images of mosaic recipient muscles showing TdTomato-positive myofibers (RFP-red) and double staining with GFP (green) and LAMININ (white). (**C-D**) Quantification of tdTomato+ myofibers number/area (**D**) and GFP+ cells from CRIPTO^Neg and CRIPTO^Pos donor cells normalized per mm² (**D**). Scale bar: 100μm. Data are mean ± SEM. Nuclei were counter-stained with DAPI. (*n*=3). (**E**) Schematic representation of the experimental design. (**F-G**)
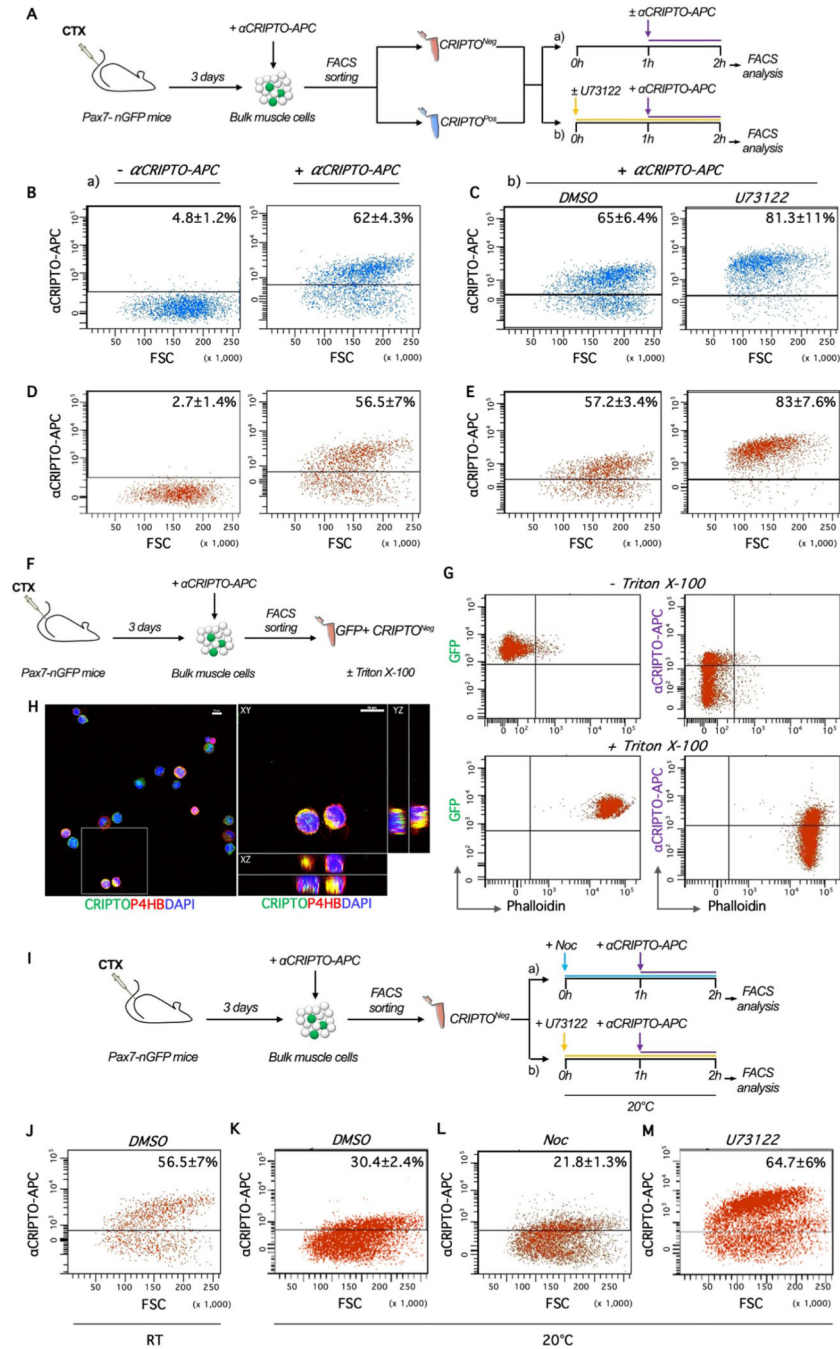
Representative dot plots of surface CRIPTO in GFP-positive CRIPTO[Neg] and CRIPTO[Pos] cells used for transplantation (**F**) and GFP-positive ASCs (3dpi) derived from CRIPTO[Neg] and CRIPTO[Pos] -transplanted mice (**G**). The percentage of CRIPTO positive cells above the threshold is indicated in the dot plots.

Figure 5. Cellular mechanisms of CRIPTO micro-heterogeneity reconstitution. See also Figure S3.

(**A**) Schematic representation of the experimental design. GFP-positive CRIPTO[Neg] and CRIPTO[Pos] ASCs were incubated at RT ± *a*CRIPTO-APC antibody (*line a*) or ± U73122 (*line b*) and stained with *a*CRIPTO-APC. (**B**-**E**) Representative dot plots of surface CRIPTO in CRIPTO[Pos] (**B** and **C**) and CRIPTO[Neg] (**D** and **E**) cells ± *a*CRIPTO-APC antibody (**B** and **D**) or ± U73122 and + *a*CRIPTO-APC (**C** and **E**). DMSO was used as Control. Data represent mean ± SEM. p   0.005 (n=5). (**F**) Schematic representation of the experimental

design. (**G**) Representative dot plots of CRIPTO and Phalloidin in not-permeabilized (−Triton X-100, upper panels) or permeabilized (+Triton X-100; bottom panels) CRIPTO[Neg] cells. Fluorescent labelled Phalloidin was used as permeabilization control. Cells were gated by either GFP or *a*CRIPTO-APC and Phalloidin. (**H**) Representative pictures and orthogonal view of confocal images of permeabilized CRIPTO[Neg] ASCs stained with anti-CRIPTO (green) and Prolyl 4-Hydroxylase Subunit Beta (P4HB, red) antibodies. Nuclei were counter-stained with DAPI. Scale bar: 50μm. The inset shows higher magnification of the boxed area (scale bar: 10μm). (**I**) Schematic representation of the experimental design. GFP-positive CRIPTO[Neg] ASCs were incubated at 20°C with either Nocodazole (Noc; *line a*) or U73122 (*line b*), and re-stained with *a*CRIPTO-APC. DMSO was used as Control. (**J-M**) Representative dot plot of surface CRIPTO in CRIPTO[Neg] ASCs incubated at RT with DMSO (**J**) or at 20°C with either DMSO (**K**), Noc (**L**) or U73122 (**M**) and re-stained with *a*CRIPTO-APC. The percentage of CRIPTO positive cells above the threshold is indicated in the dot plots. Data represent mean ± SEM. p 0.05 (n=3).
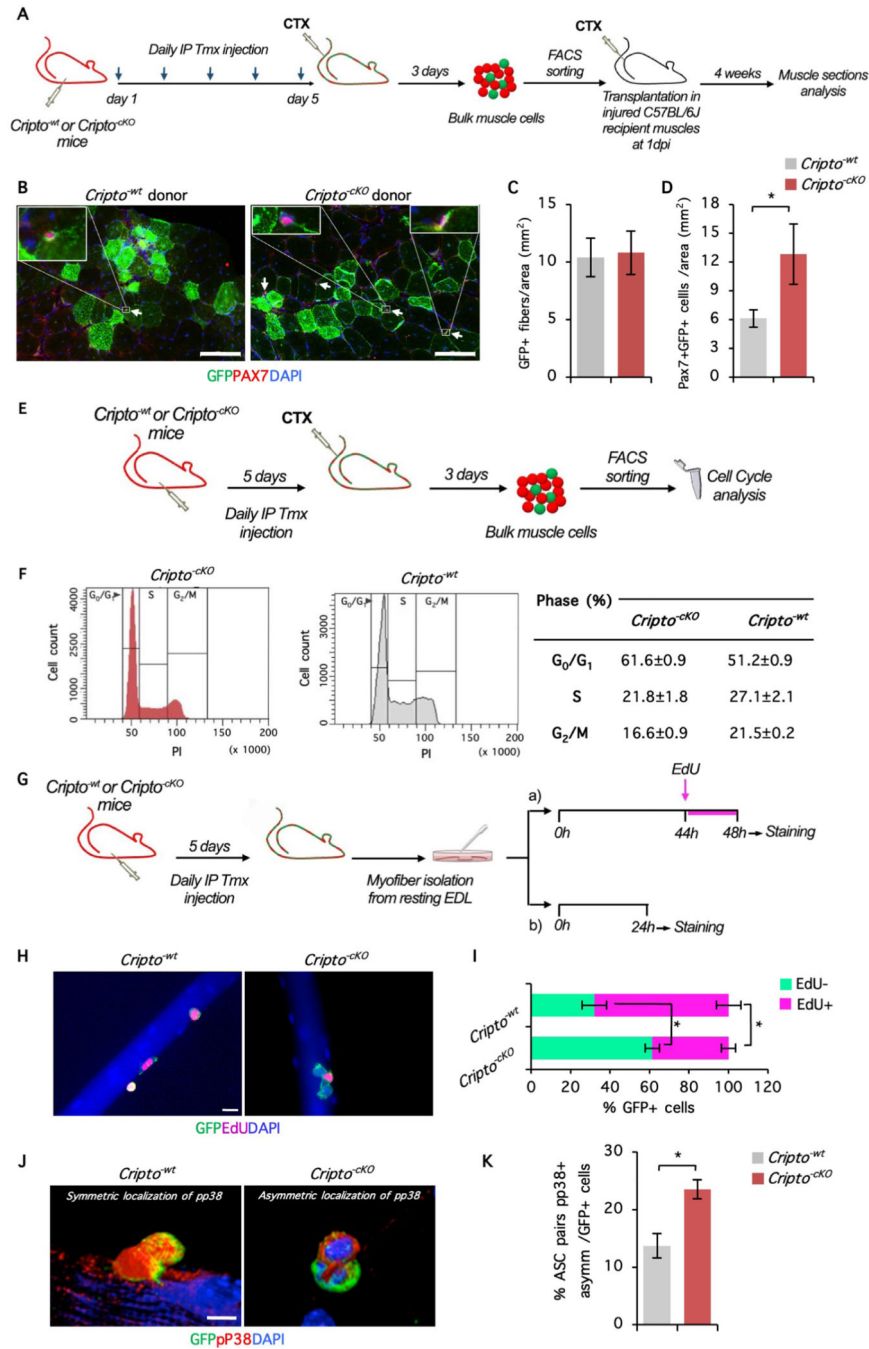
Figure 6. Permanent perturbation of CRIPTO micro-heterogeneity affects ASC behavior. See also Figure S4

(**A**) Schematic representation of the experimental design. (**B**) Representative pictures of PAX7 (magenta) and GFP (green) staining in recipient TA muscles. Nuclei were counter-stained with DAPI. Scale bar: 100μm. Insets show higher magnification (20x) of the boxed area. (**C-D**) Quantification of GFP+ myofibers number (**C**) and GFP+/PAX7+ cells (**D**) derived from *Cripto*^{-wt} and *Cripto*^{-cKO} donor cells (*n*=3). (**E**) Schematic representation of experimental design. (**F**) Representative flow cytometry histograms (left and middle panels)

and quantification (right panel) of the cell cycle distribution of *Cripto*[-wt] and *Cripto*[-cKO] cells (*n*=3). (**G**) Schematic representation of the experimental design. Floating myofibers cultured for a) 48 hours with a short EdU-pulse (4 hours) or b) 24 hours. (**H-I**) Representative pictures of EdU (magenta) and GFP (green) staining (**H**) and quantification of GFP+/EdU± ASCs–associated myofibers (**I**). Scale bar: 25μm. (**J-K**) Representative confocal images of GFP (green) and phospho-p38α/β (pP38, red) staining in *Cripto*[-wt] and *Cripto*[-cKO] ASC pairs (**J**) and quantification of asymmetric pP38 distribution in myofibers-associated ASCs pairs (**K**). (n=3 mice, >80 cells/mouse). Nuclei were counter-stained with DAPI. Data represent mean ± SEM. *p ≤ 0.05. (*n*=4).
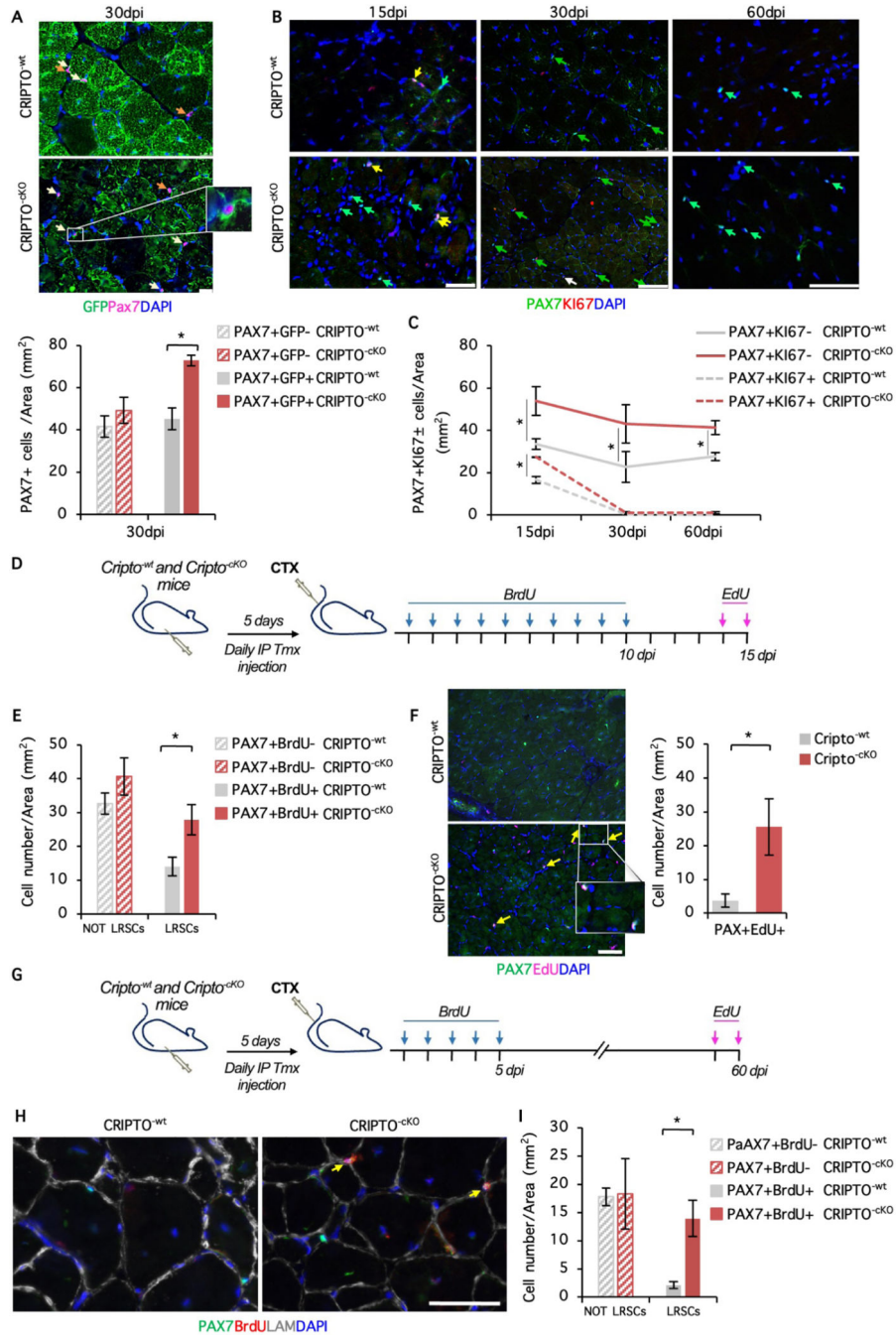
Figure 7. CRIPTO micro-heterogeneity preserves the balance between self-renewal and myogenic commitment. See also Figure S4

(**A**) Representative pictures of PAX7 (magenta) and GFP (green) staining (upper panel) and quantification of PAX7+/GFP± cells (bottom panel) in *Cripto-wt* and *Cripto-cKO* muscle sections. Inset shows higher magnification (10x) of the boxed area. Scale bar: 75μm.
(**B**) Representative pictures of PAX7 (green) and KI67 (red) staining in *Cripto-wt* and *Cripto-cKO* muscle sections at indicated time points. Yellow and green arrows indicate PAX7+/KI67+ and PAX7+/KI67− cells, respectively. Scale bar: 100μm. (**C**) Quantitative

analysis of PAX7+/KI67− (solid lines) and PAX7+KI67+ (dashed lines) -cells at indicated time points. (**D**) Schematic representation of the experimental design. BrdU and EdU were injected intraperitoneally (IP) once daily for 10 days, and at 24 and 2 hours before sacrifice, respectively. (**E**) Quantitative analysis of Label Retaining Satellite Cells (LRSCs; PAX7+/BrdU+) and Not Label Retaining Satellite Cells (NOT-LRSCs; PAX7+/BrdU−). (**F**) Representative pictures of PAX7 (green) and EdU (magenta) staining (left panel) and quantitative analysis (right panel) of PAX7+/EdU+ cells. Yellow arrows indicate PAX+/EdU+ cells. Inset shows higher magnification (5x) of the boxed area. Scale bar: 75μm. (**G**) Schematic representation of the experimental design. BrdU and EdU were injected IP once daily for 5 days, and at 24 and 2 hours before sacrifice, respectively. (**H-I**) Representative pictures of LAMININ (LAM, white), PAX7 (green) and BrdU (red) triple staining (**H**) and quantification (**I**) of PAX7+/BrdU± LRSCs and NOT-LRSCs. Yellow arrows indicate PAX+/BrdU+ cells. Scale bar: 75μm. Nuclei were counter-stained with DAPI. Data represent mean ± SEM. *p ≤ 0.05. (n=3 for 15 dpi, n=6 for 60 dpi).

KEY RESOURCES TABLE

REAGENT or RESOURCE	SOURCE	IDENTIFIER
Antibodies		
Mouse Cripto Allophycocyanin MAb	Biotechne - R&D systems	Cat# FAB1538A
Cripto Mouse specific	Cell Signaling Technology	Cat# 2818, RRID: AB_2240508
Anti-P4HB antibody [RL90]	abcam	Cat# ab2792
Pax7 Antibody	Developmental Studies Hybridoma Bank (DHSB)	Cat# PAX7, RRID: AB_528428
Anti-MyoD (C-20)	Santa Cruz Biotechnology, Inc	Cat# sc-304
Anti-GFP antibody	abcam	Cat# ab13970
Anti-human Ki67	Monosan	Cat# PSX1028
Myogenin Antibody (F5D)	Developmental Studies Hybridoma Bank (DHSB)	Cat# F5D, RRID: AB_2146602
BrdU antibody [BU1/75 (ICR1)]	GeneTex	Cat# 9216
Ki-67 Recombinant Rabbit Monoclonal Antibody (SP6)	ThermoFisher Scientific	Cat# MA5-14520
Anti-Laminin	Sigma-Aldrich	L9393
Biotin-SP (long spacer) AffiniPure Goat Anti-Mouse IgG, Fcγ subclass 1 specific	Jackson ImmunoResearch	Cat# 115-065-205, RRID: AB_2338571
Anti-mouse Alexa Fluor 549	ThermoFisher Scientific	Cat# A-21203
Anti-rabbit Alexa Fluor 488	ThermoFisher Scientific	Cat# A-11001
Anti-rabbit Alexa Fluor 555	ThermoFisher Scientific	Cat# A-31572
Anti-rabbit Alexa Fluor 549	ThermoFisher Scientific	Cat# A-21207
Alexa Fluor® 488 AffiniPure	ThermoFisher	Cat# 703-545-155, RRID: AB_2340375
Donkey Anti-Chicken IgY (IgG) (H+L)	Scientific	
Cy™3 AffiniPure Donkey Anti-Rat IgG (H+L)	Jackson ImmunoResearch	Cat# 712-165-153, RRID: AB_2340667
Chemicals, Peptides, and Recombinant Proteins		
Sambucus Nigra Lectin (SNA, EBL), Biotinylated	Vector Laboratories	Cat# B-1305-2
Rhodamine Phalloidin	ThermoFisher Scientific	Cat# R415
Streptavidin-Cy3 conjugated	Jackson ImmunoResearch	Cat# 016-160-084
Streptavidin-488 conjugated	Invitrogen	Cat# S32354
Streptavidin-647 conjugated	Invitrogen	Cat# 532357
Tamoxifene	Sigma-Aldrich	Cat# T5648
Cardiotoxin	Latoxan Laboratory	Cat# L8102
Dispase II	Roche	Cat# 10887800
Collagenase A	Roche	Cat# 10103586001
DNAse I	Roche	Cat# 11284932001
Hank's Balanced Salt Solution (HBSS)	Gibco	Cat# 14170-088
Bovine Serum Albumin (BSA)	Sigma-Aldrich	Cat# A4503
Penicillin-Streptomycin	Gibco	Cat# 15140-122

REAGENT or RESOURCE	SOURCE	IDENTIFIER
Collagenase	Sigma-Aldrich	Cat# C0130
Dulbecco's Modified Eagle's medium (DMEM)	Gibco	Cat# 41965-039
Ham's F-12 Nutrient Mix, GlutaMAX™	Gibco	Cat# 31765-027
Pyruvate Sodium	Gibco	Cat# 11360-039
L-Glutamine 200mM (100x)	Gibco	Cat# 25030-024
Fetal Bovine Serum (FBS)	Euroclone	Cat# ECS5000L
Ultroser G	Sartorius	Cat# 15950-017
Goat Serum	Merck	Cat# G9023
Nocodazole	Sigma-Aldrich	Cat# M1404
U73122	Selleckchem	Cat# S8011
Varespladib (LY315920)	Selleckchem	Cat# S1110
FIPI	Selleckchem	Cat# S7321
Trizol Reagent	Invitrogen	Cat# 15596018
SYBR Green PCR master mix (FluoCycle II™ SYBR®)	EuroClone	Cat#ERD002250BIM
BD Matrigel™ Basement Membrane Matrix	BD Biosciences	Cat# 354234
5-bromo-2'deossiuridina (BrdU)	Sigma-Aldrich	Cat# B5002
Bovine Serum Albumin (IgG Free, Protease Free)	Jackson ImmunoResearch	Cat# 001-000-162
AffiniPure Fab Fragment goat anti-mouse IgG	Jackson ImmunoResearch	Cat# 115-007-003
FluorSave Reagent	Calbiochem	Cat# 345789
Critical Commercial Assays		
MitoTracker Orange CM-H2TMRos	ThermoFisher Scientific	Cat# M7511
Wizard® Genomic DNA Purification kit	Promega	Cat# A1120
MethylFlashTM Global DNA Hydroxymethylation (5hmC) ELISA Easy Kit	Epigentek	Cat# P-1032-96
Direct-Zol Microprep kit	Zimo-Research	Cat# R2060
QuantiTect Reverse Transcription Kit	Qiagen	Cat# 205311
Click-iT EdU Alexa Fluor 647 imaging kit	Invitrogen	Cat# C10340
Deposited Data		
Raw RNA-seq data	This paper	SRA: PRJNA637587
Experimental Models: Organisms/Strains		
Mouse: Tg:Pax7-nGFP	The Jackson Laboratories	MGI:5308730
Mouse: C57BL/6	Charles River	C57BL/6 mice
Mouse: Tg:Pax7-nGFP::R26^{mTmG}	This paper	N.A.
Mouse: Tg:Pax7-CreERT2::R26^{mTmG}::Cripto$^{loxP/-}$	This paper	N.A.
Mouse: Tg:Pax7-CreERT2::R26^{mTmG}	This paper	N.A.
Oligonucleotides		
See Table S2 for list of oligonucleotides	This paper	N.A.
Software and Algorithms		
BD FACSDiva software	BD Biosciences	N.A.

REAGENT or RESOURCE	SOURCE	IDENTIFIER
DAVID Functional Annotation Tool 6.8	LHRI	https://david.ncifcrf.gov/
GSEA v3.0	UC San Diego - BROAD Institute	https://www.gsea-msigdb.org/gsea/index.jsp
Fiji Software	NIH	https://hpc.nih.gov/apps/Fiji.html
R Studio	Posit	https://posit.co/download/rstudio-desktop/
Photoshop	Adobe	https://www.adobe.com/it/products/photoshop.html
Biorender	biorender	https://www.biorender.com/
ImageJ	NIH	https://imagej.nih.gov/ij/
FASTQC v0.11.3	Babraham Bioinformatics	http://www.bioinformatics.babraham.ac.uk/projects/fastqc/
Trimmomatic v0.36	Bolger et al., 2014 [53]	http://www.usadellab.org/cms/?page=trimmomatic
STAR v2.5.2a	Dobin et al., 2013 [54]	https://github.com/alexdobin/STAR
HTSeq v0.6.1p1	Anders et al., 2015 [56]	https://htseq.readthedocs.io/en/release_0.11.1/index.html
DESeq2 v1.20.0	Love et al., 2014 [57]	https://bioconductor.org/packages/release/bioc/html/DESeq2.html